energies

MDPI

Article

Ternary Fe- or Mo-Au-Ni/GDC as Candidate Fuel Electrodes for the Internal Dry Reforming of CH_4: Physicochemical and Kinetic Investigation

Evangelia Ioannidou [1,*], Stylianos G. Neophytides [1] and Dimitrios K. Niakolas [1,2,*]

[1] Institute of Chemical Engineering Sciences, Foundation for Research and Technology-Hellas (FORTH/ICE-HT), GR-26504 Patras, Greece; neoph@iceht.forth.gr
[2] Department of Chemistry, University of Ioannina, GR-45110 Ioannina, Greece
* Correspondence: niakolas@iceht.forth.gr (D.K.N.); eioannidou@iceht.forth.gr (E.I.)

Abstract: The present study deals with the physicochemical and catalytic/kinetic investigation of Fe, Au, Fe-Au, and Mo-Au modified Ni/GDC electrocatalysts towards their performance for the DRM, RWGS, and CH_4 decomposition reactions. For this purpose, Au-NiO/GDC (where Au = 1 or 3 wt.%), Fe-NiO/GDC (where Fe = 0.5 or 2 wt.%), 0.5Fe-3Au-NiO/GDC, and 0.4Mo-3Au-NiO/GDC were synthesized via deposition (co-) precipitation. There is discussion on the structural properties of the electrocatalysts on the oxidized and reduced state, as well as their use as electrolyte-supported (half) cells. A key remark after H_2-reduction is the formation of binary or ternary solid solutions. Ni/GDC was the most active for the catalytic CO_2 reforming of CH_4 and the CH_4 decomposition reactions and as a result the most prone to carbon deposition. On the other hand, the modified 3Au-Ni/GDC, 0.5Fe-3Au-Ni/GDC, and 0.4Mo-3Au-Ni/GDC exhibited the following properties: (i) the highest $E_{a,app}$ for the non-desired RWGS reaction, (ii) high tolerance to carbon formation due to lower activity for the CH_4 decomposition, and (iii) were also less active for H_2 and CO production. Finally, 0.4Mo-3Au-Ni/GDC seems to perform the DRM reaction through a different mechanism when compared to Ni/GDC. Overall, the above three samples are proposed as potential fuel electrodes for further electrocatalytic measurements for the SOFC internal DRM process.

Keywords: SOFCs; DRM; RWGS; carbon deposition; reaction kinetics; Mo-Au-Fe-Ni/GDC electrocatalysts; internal dry reforming of CH_4

Citation: Ioannidou, E.; Neophytides, S.G.; Niakolas, D.K. Ternary Fe- or Mo-Au-Ni/GDC as Candidate Fuel Electrodes for the Internal Dry Reforming of CH_4: Physicochemical and Kinetic Investigation. *Energies* **2024**, *17*, 184. https://doi.org/10.3390/en17010184

Academic Editor: Philippe Leclère

Received: 16 November 2023
Revised: 12 December 2023
Accepted: 24 December 2023
Published: 28 December 2023

1. Introduction

Recycling CO_2 and CH_4 to produce syngas (H_2 + CO) through Dry Reforming of Methane (DRM) has received considerable attention and prominent research interest. CO_2 and CH_4 are greenhouse gases and the main compounds of biogas (55–65% CH_4 and 45–55% CO_2), which is widely produced by anaerobic fermentation of biomass [1]. The DRM process offers a feasible solution to abate CO_2 and CH_4, responsible for global warming and major climate changes, via production of synthesis gas (or syngas) with a molar H_2/CO ratio close to unity [2,3]. Furthermore, the syngas from DRM is suitable for further usage and synthesis of long-chain hydrocarbons in the Fischer-Tropsch industry [4,5].

Among the existing technologies for DRM energy applications, high temperature (750–1000 °C) Solid Oxide Fuel Cells (SOFCs) are the most efficient devices for electricity production [6–9]. A SOFC fed by biogas can operate either by using an external reformer, which converts the biogas to syngas, or without using an external reformer, inside the fuel cell, by utilizing advanced fuel electrodes [10,11]. The first approach represents the State of the Art (SoA) of the current technology, where the external reformer converts biogas to syngas and then this stream is fed to the fuel side of SOFC [6,11,12]. The second approach which is also known as "internal dry reforming of methane (IDRM)" uses modified improved electrodes to convert biogas to syngas through a catalytic DRM reaction and

then to electricity through charge transfer reactions inside the SOFC [4,10,13–15]. The main advantages of this concept include simplified system design without external reformer and reduced air-flow/energy-losses because the heat released by the exothermic charge transfer reactions can also be used for the endothermic catalytic reactions (DRM, etc.) [10,14–17].

In general, when SOFCs operate at temperatures of 750–900 °C under internal dry reforming of methane conditions, several (electro)catalytic reactions may occur simultaneously on the fuel electrode (Equations (1)–(6)) [1,10,11,16,18,19]. In this respect, in the fuel side CO_2 and CH_4 are converted into H_2 and CO via the DRM reaction (Equation (1)). Due to the strongly endothermic character of DRM, high reaction temperatures (>750 °C) are required to achieve high H_2 and CO yields [3,4].

$$CH_4 + CO_2 \leftrightarrow 2CO + 2H_2 \quad \Delta H^{o}_{1073} = 260 \text{ kJ mol}^{-1} \tag{1}$$

During operation, the produced H_2 from the DRM may be consumed through the Reverse Water Gas Shift (RWGS) reaction (Equation (2)), resulting in decreased H_2/CO ratio values (<1) [20].

$$CO_2 + H_2 \leftrightarrow CO + H_2O \quad \Delta H^{o}_{1073} = 41 \text{ kJ mol}^{-1} \tag{2}$$

Moreover, carbon deposition on the surface of the electrocatalyst may occur through cracking of CH_4 (Equation (3)), and this is a very important issue since it is responsible for the progressive electrocatalyst deactivation [20,21]. The CH_4 decomposition reaction (Equation (3)) is thermodynamically favored at the high temperature region of >600 °C, whereas at lower temperatures (<650 °C) carbon is mainly produced through the CO disproportionation (Boudouard) reaction ($2CO \rightarrow C + CO_2$) [20–22].

$$CH_4 \leftrightarrow C + 2H_2 \quad \Delta H^{o}_{1073} = 85 \text{ kJ mol}^{-1} \tag{3}$$

During fuel cell operating conditions, the produced H_2 and CO, as well as the supplied CH_4 can be electrochemically oxidized in the triple phase boundary (TPB) region by oxygen ions (O^{2-}) to produce power, according to Equations (4)–(6) [23–27].

$$H_2 + O^{2-} \leftrightarrow H_2O + 2e^- \quad \Delta H^{o}_{1073} = -152 \text{ kJ mol}^{-1} \tag{4}$$

$$CO + O^{2-} \leftrightarrow CO_2 + 2e^- \quad \Delta H^{o}_{1073} = -186 \text{ kJ mol}^{-1} \tag{5}$$

$$CH_4 + O^{2-} \leftrightarrow CO + 2H_2 + 2e^- \quad \Delta H^{o}_{1023} = -22 \text{ kJ mol}^{-1} \tag{6}$$

Although significant progress has been made on the development of advanced SOFC systems, the main issue that hinders the commercialization of this technology, particularly under CH_4 reforming processes, is the performance degradation of the cells and especially of the fuel electrodes. The performance of cells/fuel electrodes is affected by the thermal stresses resulting from the endothermic (Equations (1)–(3)) and the exothermic (Equations (4)–(6)) (electro)catalytic reactions, as well as the chemical degradation due to coke formation [19].

The State-Of-the-Art (SoA) electrocatalysts in SOFCs are Ni-ceramic-metal composites comprising Yttria Stabilized Zirconia (YSZ) and Gadolinia Doped Ceria (GDC), due to their excellent activity for electrochemical reactions and low cost [28,29]. In this respect, Ni/GDC is widely used as a fuel electrode, since it exhibits higher catalytic performance in CH_4 reforming reactions and resistance to coke formation when compared to Ni/YSZ electrodes [19,30,31]. The improved performance of Ni/GDC is attributed to the capacity of ceria to store and release oxygen. This property favours the oxidation and thus the removal of surface carbon species and the oxidation of CH_4 instead of its decomposition [19,32]. An alternative solution to suppress the carbon deposition and sintering tendency of nickel can be achieved by dispersing small amounts of transition noble (Ru, Rh, Pd, Pt, Au) or non-noble (Fe, Co, Cu, Mo, W) metals [1,16,32].

In the same direction, our research group has studied the effect of Au and/or Mo or Fe addition on commercial NiO/GDC powder in solid oxide applications [33–37]. The modifications have so far resulted in electrocatalysts with enhanced electrochemical performance and tolerance against nickel oxidation and carbon or sulphur poisoning under steam (or steam + CO_2) electrolysis [35–37] and under internal steam reforming of methane (ISRM) operating conditions in the presence/absence of 10 ppm H_2S [33,34]. In these studies, the modified cermets exhibited variations in their physicochemical and electrochemical properties, which were correlated with the formation of bimetallic Fe-Ni, Au-Ni, and ternary Mo–Au–Ni solid solutions during the H_2-reduction process. According to the ISRM studies, 0.4Mo-3Au-Ni/GDC was found to be the most carbon tolerant electrode when compared to Ni/GDC, 0.4Mo-Ni/GDC, and 3Au-Ni/GDC under both helium diluted or non-diluted harsh H_2O/CH_4 reaction feed conditions [34]. The improved performance of 0.4Mo-3Au-Ni/GDC was ascribed to the inhibited complete dehydrogenation of methyl species (CH_x) towards carbon on the active sites of the electrode [32]. Although Au utilization is not cost-effective compared to non-precious metals, its usage may be compensated if long-term operation and carbon tolerance is achieved.

In regards to the substitution of noble metals, iron is indicated as a promising transition metal dopant of Ni, due to its improved redox properties, its abundancy, and its lower price. The first research efforts of our group focused on the modification of Ni/GDC with various wt.% Fe with quite promising results for the solid oxide steam electrolysis reaction [37]. Notably, 0.5Fe-Ni/GDC displayed the highest performance compared to Ni/GDC and 2Fe-Ni/GDC, whereas the main problem was the poor stability that resulted in the decrease in the electrocatalytic activity. The CO_2 reforming of CH_4 has also been studied over Fe-Ni-based catalysts, focusing on the synergistic interaction of Fe-Ni towards the DRM activity and carbon formation propensity. According to some of the above research studies [38–42], under DRM reaction conditions FeO_x species are formed due to partial segregation of metallic Fe from the Fe-Ni alloyed particles, favouring the interaction of FeO_x with the accumulated carbon towards its gasification. A recent study over Fe-Ni/MgO catalysts [43] showed that Fe modification can inhibit carbon deposition under DRM reaction conditions, but at the same time may alter the nature of the deposited carbon towards a form that can be easily removed from the catalyst surface via gasification by CO_2.

In the present work, the performance of the following electrocatalysts (Ni/GDC, 1 wt.% Au-Ni/GDC, 3 wt.% Au-Ni/GDC, 0.5 wt.% Fe-Ni/GDC, 2 wt.% Fe-Ni/GDC, 0.5 wt.% Fe-3 wt.% Au-Ni/GDC, and 0.4 wt.% Mo-3 wt.% Au-Ni/GDC) was evaluated at Open Circuit Potential (OCP) conditions under biogas fuel operation. The samples were tested in the form of Electrolyte Supported (half) Cells (ESCs) at 750–900 °C by applying a reaction fuel mixture of CH_4/CO_2 = 1 with inlet gas flows that varied in the range between 150 to 300 cm^3/min. The latter approach provided a reference profile for the catalytic performance of the candidate electrocatalysts by applying the same CH_4/CO_2 fuel feed conditions as those under IDRM operational mode but without the effect of applied current/potential. In addition, selected samples were further studied through specific kinetic measurements under differential conditions at various CH_4 and CO_2 partial pressures in an attempt to clarify the effect of modification on the intrinsic catalytic activity of Ni/GDC for the DRM reaction. The research objective of this investigation focuses on the sustainable conversion of the greenhouse CH_4 and CO_2 gases towards syngas by means of Solid Oxide Fuel cells, which is a highly efficient and environmentally friendly electrochemical source of energy/power and useful chemicals.

2. Experimental

2.1. Preparation of Powders

The modified powders were prepared via the Deposition—Precipitation (D.P.) and Deposition—Co Precipitation (D.CP.) methods by using the commercial NiO/GDC cermet (65 wt.% NiO-35 wt.% GDC, Marion Technologies) as the support. The precursors for the 1 wt.% Au-Ni/GDC, 3 wt.% Au-Ni/GDC, 0.5 wt.% Fe-Ni/GDC, 2 wt.% Fe-Ni/GDC,

0.5 wt.% Fe-3 wt.% Au-Ni/GDC, and 0.4 wt.% Mo-3 wt.% Au-Ni/GDC samples were $HAuCl_4$ (99.99% trace metals basis, 30 wt.% in dilute HCl), $Fe(NO_3)_3x9H_2O$ (ACS reagent $\geq$ 98%), and $(NH_4)_6Mo_7O_{24}$ (99.98% metals basis) purchased from Sigma-Aldrich (St. Louis, MO, USA). Full details about the synthesis of the electrocatalysts can be found elsewhere [33,37]. During the process, the temperature was fixed at 70 °C and pH was adjusted by using NH_3 (1 M), at 7.0 for Au-NiO/GDC, 8.0 for Fe-NiO/GDC, and 6.0 for Fe-Au-NiO/GDC and Mo-Au-NiO/GDC samples. In the case of Au-modified electrocatalysts, after filtering the precipitate was mildly washed in order to eliminate any residual Cl^-. Finally, in all cases, the precipitate was dried at 110 °C for 24 h and then each powder was calcined in air at 600 °C/90 min and a part of it at 1100 °C/75 min. The first batch was used for the preparation of a paste for electrode production and the last one for physicochemical characterization. Calcination at 1100 °C is considered necessary in order to examine the powders at similar calcination conditions, such as those where the cells are prepared. In the following sections, the examined samples will be reported as 1Au-NiO/GDC, 3Au-NiO/GDC, 0.5Fe-NiO/GDC, 2Fe-NiO/GDC, 0.5Fe-3Au-NiO/GDC, and 0.4Mo-3Au-NiO/GDC.

2.2. Preparation of Half Cells

The half cells were supported on a circular shaped planar 8YSZ electrolyte with 25 mm diameter and 300 μm thickness, purchased from Kerafol. As reported in previous studies [34,36], the deposition of the electrode was made by using the screen-printing method and a paste which consisted of a proper amount of calcined powder at 600 °C, terpineol as the dispersant, and PVB (polyvinylbutyral) as the binder, purchased from Sigma-Aldrich. After the paste-deposition, the cell was sintered at 1150 °C with a heating/cooling ramp rate of 2 °C/min. The loading of the examined fuel electrodes was ~6 mg cm^{-2} and the active surface area was 1.8 cm^2.

2.3. Physicochemical Characterization

The powders, in their oxidized and H_2-reduced form, were characterized with XRF (X-ray Fluorescence), BET (Brunauer-Emmett-Teller), XRD (X-ray Diffraction), and TGA (Thermogravimetric Analysis) in the presence of CH_4. Specifically, the elemental wt.% concentration in each sample was determined by means of the non-destructive X-ray fluorescence (XRF) analysis using a portable Bruker Tracer III SD set with a beam diameter of 3 mm. The BET Specific Surface Area values (SSAs) were measured with a Micromeritics TriStar 3000 apparatus, employing nitrogen physisorption at the temperature of liquid nitrogen (77 K). In each measurement, the sample was pre-heated and outgased under dynamic vacuum at 250 °C for 2 h.

XRD measurements were performed by using a Bruker D8 Advance instrument equipped with a nickel-filtered Cu Kα (0.15418 nm) radiation source. The step size and the time per step were respectively fixed at 0.02° and 5 s, in the range of $20° \leq 2\theta \leq 60°$. The patterns were analyzed via the DiffracPlus-EVA software. The peaks were identified by using the standard reference crystallographic patterns of NiO: 044-1159, Ni: 004-0850, GDC: 046-0508, Au: 065-2870, and Fe_2O_3: 039-1346. The primary crystallite size of the main detected nanocrystals was estimated by means of Scherrer's formula:

$$d = \frac{0.9\lambda}{B\cos\theta} \quad (7)$$

where λ is the X-ray wavelength corresponding to Cu Kα radiation (0.15418 nm), θ is the diffraction angle, and B is the line broadening (in radians) at half maximum. For the estimation of the d values, the diffraction peaks that were used are located at 2θ equal to 43.4° for NiO (0 1 2), 44.4° for Ni (1 1 1), 28.6° for GDC (2 2 2), 38.1° for Au (1 1 1), and 35.6° for Fe_2O_3 (3 1 1).

TGA measurements were performed in a TA Q50 instrument isothermally at 800 °C under 10 vol.% CH_4/Ar with a total flow rate of 100 cm^3 min^{-1}. The weight of each sample

was ~25 mg and before the measurement the powder was reduced in-situ with 80 vol.% H_2/Ar at 800 °C for 100 min. After the H_2-reduction period, the reaction mixture was switched and CH_4/Ar was added in the feed.

2.4. Catalytic/Kinetic Measurements

The electrolyte-supported half cells were attached on a YSZ tube-reactor and were sealed airtight by using a glass sealing material. The half cells were investigated catalytically at OCP conditions under biogas fuel operation. The experiments were performed in the presence of a Ni mesh at 750–900 °C under a fuel mixture with CH_4/CO_2 = 1 without dilution in a carrier gas. Specifically, four experimental cycles were performed per temperature. Each cycle consisted of a total inlet gas flow ranging between 150–300 cm^3/min with a step of 50 cm^3/min, while the operating temperature was fixed. By changing the cycle, the experimental procedure was the same, but the temperature varied from 750 to 900 °C with a step of 50 °C. The kinetic measurements were carried out under differential conditions at various CH_4 and CO_2 partial pressures. Reactants and products were detected by using an on-line gas chromatograph (Varian CP-3800) with a thermal conductivity detector. A Porapak Q column (80–100 mesh, 1.8 m × 1/8 in. × 2 mm) was used for the analysis of H_2O at 150 °C while a Carbosieve S-11 column (80–100 mesh, 2 m × 1/8 in. × 2 mm) was used for the analysis of H_2, CO, CH_4, and CO_2 (in parallel with the Porapak Q).

The catalytic rates of reactants and products were calculated through Equation (8) and the carbon formation rates were determined by using the measured production rates of H_2, H_2O, and CO in the mass balance equation of carbon (Equation (9)).

$$r_i\left[\frac{mol}{s}\right] = \frac{F\left[\frac{cm^3}{min}\right] * (C_{i,in} - C_{i,out})}{V_m * 60\left[\frac{s}{min}\right]} \quad (8)$$

where r_i is the consumption/production rate for H_2O, H_2, CO, CH_4 and CO_2, F is the total volumetric flow, V_m is the molecular volume of ideal gases (24,451 $\frac{cm^3}{mol}$ at 25 °C and 1 atm), $C_{i,in}$ and $C_{i,out}$ $\left[\frac{cm^3}{min}\right]$ are the reactor inlet/outlet concentrations of each compound, respectively.

$$r_C\left[\frac{mol}{s}\right] = \frac{r_{H_2} + 2r_{H_2O} - r_{CO}}{2} \quad (9)$$

The corresponding % conversions of the reactants (CH_4, CO_2) were calculated according to Equations (10) and (11).

$$\%CH_4 \text{ Conversion} = \frac{CH_{4,in} - CH_{4,out}}{CH_{4,in}} \quad (10)$$

$$\%CO_2 \text{ Conversion} = \frac{CO_{2,in} - CO_{2,out}}{CO_{2,in}} \quad (11)$$

3. Results and Discussion

Physicochemical Characterization

The wt.% amount of each dopant (Mo, Fe, or Au) in the total mass of the oxidized NiO/GDC powder was investigated by means of XRF analysis and the results confirmed that the calculated wt.% loadings are close to the nominal values which are presented in Table 1.

The Specific Surface Area (SSA) values of modified cermets, in their oxidized and reduced form, are presented in Table 2.

Table 1. XRF analysis of the Mo, Au, and Fe wt.% concentration on the examined oxidized powders after calcination at 1100 °C.

Sample	wt.% Concentration		
	Mo	**Au**	**Fe**
1Au-NiO/GDC	–	0.8	–
3Au-NiO/GDC	–	2.7	–
0.5Fe-NiO/GDC	–	–	0.5
2Fe-NiO/GDC	–	–	2.1
0.5Fe-3Au-NiO/GDC	–	2.5	0.6
0.4Mo-3Au-NiO/GDC	0.7	2.6	–

Table 2. Specific Surface Area (SSA) values determined with the BET method of the calcined powders in their oxidized and reduced form. Error/accuracy = ± 0.2 m^2 g^{-1}.

Sample	SSA (m^2 g^{-1})	
	T = 1100 °C, (Oxidized)	**After H_2-Reduction at T = 900 °C/2 h**
NiO/GDC	4.2	2.5
1Au-NiO/GDC	4.3	2.2
3Au-NiO/GDC	2.7	2.1
0.5Fe-NiO/GDC	3.4	3.1
2Fe-NiO/GDC	4.0	3.4
0.5Fe-3Au-NiO/GDC	3.9	2.1
0.4Mo-3Au-NiO/GDC	2.8	2.3

Concerning the effect of the dopants, and by considering the error/accuracy limit of BET measurements on these materials (± 0.2 m^2 g^{-1}), the addition of 3 wt.% Au, with or without 0.4 wt.% Mo, caused a ~33% decrease in the SSA of the oxidized NiO/GDC, whereas in the H_2-reduced form there was no difference in the SSA of Ni/GDC. Interestingly and opposite to the case of Mo/Au, the addition of Fe caused an increase in the SSA value. Specifically, this was ~24% and ~36% for 0.5Fe-Ni/GDC and 2Fe-Ni/GDC, respectively. The beneficial effect of Fe addition in inhibiting the decrease in $SSA_{Ni/GDC}$ upon H_2-reduction was also reported in previous studies [36,37]. Another remark refers to the SSA of the oxidized ternary 0.5Fe-3Au-NiO/GDC sample, which exhibited higher value than that of 0.5Fe-NiO/GDC and 3Au-NiO/GDC. This can be realized via a synergistic interaction between the co-deposited Fe and Au dopants with NiO/GDC, which seems to retain the SSA of the specific sample. However, upon H_2-reduction the SSA decreased to a similar value like that in the majority of the examined samples.

The effect of modifiers on the bulk phase of NiO/GDC powder was further studied by means of XRD analysis. Figure 1 and Figure S1A in the Supplementary Materials present the XRD patterns of cermets calcined at 1100 °C. Typical diffraction peaks of NiO (JCPDS 044-1159) and GDC $(Gd_{0.6}Ce_{0.4})_2O_{3.2}$ (JCPDS 046-0508) phases were detected in all samples. It is worth mentioning that the diffraction peaks of NiO and GDC appeared at the same 2θ position for all samples and no displacement was observed, as it can be seen in the magnification of the main peaks for NiO (0 1 2) and GDC (2 2 2) in the regions ($42.8° \leq 2\theta \leq 43.6°$) and ($28° \leq 2\theta \leq 28.8°$), respectively (Figure S1B,C in the Supplementary Materials).

Iron was detected in the form of maghemite-C, syn-Fe_2O_3 (JCPDS 039-1346), only for the 2Fe-NiO/GDC sample with three peaks at $2\theta = 30.2°$ for the plane (2 2 0), 35.6° for (3 1 1), and 57.3° for (5 1 1). The absence of Fe_2O_3 diffraction peaks in the 0.5Fe-NiO/GDC and 0.5Fe-3Au-NiO/GDC samples can be attributed to the low wt.% content of iron which is below the detection limit of the XRD technique.

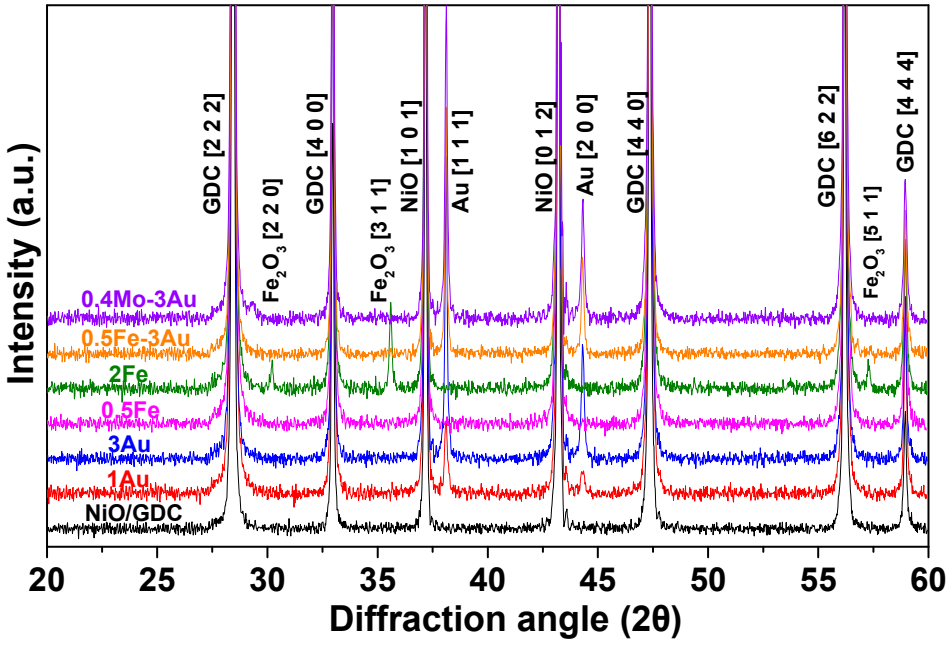

Figure 1. XRD patterns of the oxidized Mo-Au-Fe-NiO/GDC powders after calcination in air at 1100 °C/75 min. Reflections indexed are shown in brackets.

Moreover, gold was detected in the form of metallic Au (JCPDS 065-2870) with two peaks at 2θ = 38.1° for the plane (1 1 1) and 44.3° for (2 0 0). Concerning molybdenum, the XRD pattern of 0.4Mo-3Au-NiO/GDC highlighted its possible absence as MoO_x bulk particles. Complementary results from previous XRD and "quasi" in-situ (H_2 or H_2O) XPS analysis on Au or/and Mo and Mo-Au-NiO/GDC samples [33,35,44] confirm the above XRD analysis, but also highlight the presence of molybdate species on the surface of the oxidized 0.4Mo-3Au-NiO/GDC sample, which interact with Ni (or Ni-Au) upon H_2-reduction towards the formation of a Mo-Au-Ni solid solution.

The corresponding XRD patterns of the H_2-reduced powders at 900 °C for 2 h are presented in Figure 2A and Figure S1D in the Supplementary Materials. Two magnified areas of the main diffraction peaks of Ni (syn-Ni, JCPDS 004-0850) with the plane (1 1 1) and GDC (JCPDS 046-0508) with the plane (2 2 2) are also presented in Figures 2B and 2C, respectively. It is observed that after H_2-reduction at 900 °C, both iron and gold were not detected in the XRD patterns of the samples, suggesting their possible absence in the bulk phase of the samples, as well as a re-arrangement in the structure of the reduced materials.

More specifically, the absence of bulk iron particles in 2Fe-Ni/GDC is confirmed by a shift of the Ni diffraction peaks to lower 2θ values, indicating the formation of a Ni-Fe solid solution during H_2-reduction, which is further confirmed by previous studies in the literature [37,45–48] (Figure 2B). This shift in the present study can be realized through the detection of a shoulder at 44.3° of the main diffraction peak Ni (1 1 1), which at this point is ascribed to Ni-2Fe solid solution and is currently under further evaluation. The latter effect is also detectable in the XRD pattern of 0.5Fe-Ni/GDC, where Ni (1 1 1) was slightly shifted.

Similarly, an absence of bulk gold particles was observed in 1Au-Ni/GDC, 3Au-Ni/GDC, 0.5Fe-3Au-Ni/GDC, and 0.4Mo-3Au-Ni/GDC, which was further verified by a shift of the Ni diffraction peaks to lower 2θ values, indicating the formation of Ni-Au or Ni-Fe-Au and Ni-Mo-Au solid solutions during the H_2-reduction process. Particularly, Ni-Au and Ni-Mo-Au solid solutions in Ni/YSZ and Ni/GDC cermets have been thoroughly reported in previous studies of our research group [33,35].

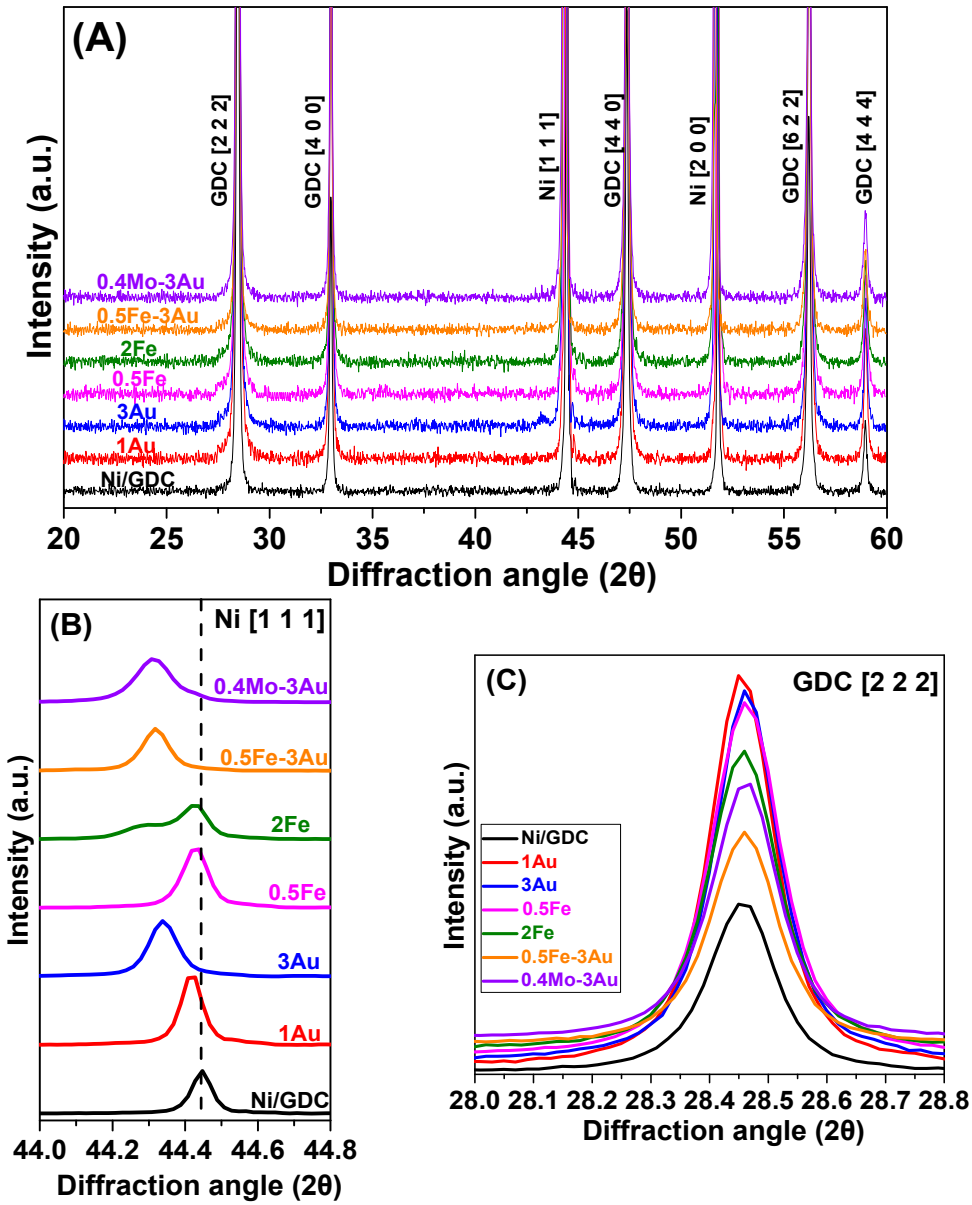

Figure 2. XRD patterns of Mo-Au-Fe-Ni/GDC powders after H_2-reduction at 900 °C. Specifically, there are depictions of the (**A**) whole pattern, (**B**) magnification of the Ni (1 1 1) peak in the range of $44.0° \leq 2\theta \leq 44.8°$, (**C**) magnification of the GDC (2 2 2) peak in the range of $28.0° \leq 2\theta \leq 28.8°$. Reflections indexed are shown in brackets.

Concerning the Ni-Fe-Au solid solution, this is the first time that it is studied by means of XRD measurements. Specifically, the incorporation of the larger atomic radius ions of Fe (1.56 Å) or/and Au (1.74 Å) or/and Mo (1.90 Å) into the Ni (1.49 Å) [49] lattice has been reported to cause an increase in the crystal lattice parameter value of the Ni-Fe, Ni-Au, Ni-Fe-Au, and Ni-Mo-Au phases [33,45,50,51]. The lattice parameters for the above solid solution phases were calculated by the (1 1 1) diffraction plane of Ni (Figure 2B) via the DiffracPlus-EVA software. In particular, the lattice parameter values were estimated as equal to 3.530 Å for Ni, 3.532 Å for 1Au-Ni, 3.539 Å for 3Au-Ni, 3.532 Å for 0.5Fe-Ni, and 3.540 Å for 2Fe-Ni, 0.5Fe-3Au-Ni, and 0.4Mo-3Au-Ni. On the other hand, it should be mentioned that no shift was detected for the GDC diffraction peaks, as it can be seen in the magnification of the main peak of GDC (2 2 2) (Figure 2C).

The mean primary size (d) of the detected nanocrystals in the XRD patterns was estimated from the main peaks of NiO (0 1 2), Ni (1 1 1), GDC (2 2 2), Fe_2O_3 (3 1 1), and

Au (1 1 1), according to the Scherrer equation (Equation (7)). The calculated values for the oxidized and reduced samples are presented in Table 3. More specifically, the crystal size of GDC did not change after calcination or H_2-reduction or after Fe, Au, and Mo modification, with a mean diameter of ~65 nm. Moreover, the crystallite size of NiO showed minor deviation (~15% increase) upon modification with Fe or/and Au, whereas a ~37% increase was observed upon modification with 0.4 wt.% Mo and 3 wt.% Au in the oxidized samples. Finally, by increasing the loading of Au from 1 to 3 wt.%, the Au crystal size increased by 34% and this value did not change upon addition of 0.5 wt.% Fe or 0.4 wt.% Mo. On the other hand, a decrease in the Ni crystallite size was detected on the H_2-reduced samples. Specifically, the primary size of Ni decreased by 12% and 31% in the cases of 1Au-Ni/GDC and 3Au-Ni/GDC, by 24% and 40% in 0.5Fe-Ni/GDC and 2Fe-Ni/GDC, and by 24% and 45% in 0.5Fe-3Au-Ni/GDC and 0.4Mo-3Au-Ni/GDC.

Table 3. Primary, mean, crystallite size (nm) of NiO, Ni, GDC, Fe_2O_3, and Au, estimated from XRD line broadening and by using the Scherrer equation (Equation (7)), for Mo-Au-Fe-NiO/GDC electrocatalysts in their oxidized and reduced form.

	Primary, Mean, Crystallite Size, d, (nm)						
	NiO/GDC	**1Au**	**3Au**	**0.5Fe**	**2Fe**	**0.5Fe-3Au**	**0.4Mo-3Au**
	Oxidized, calcined at T = 1100 °C						
NiO	98	116	119	113	106	111	134
GDC	67	67	70	69	65	71	69
Au	–	56	75	–	–	83	72
Fe_2O_3	–	–	–	–	67	–	–
	After H_2-reduction at T = 900 °C						
Ni	132	116	91	100	79	100	73
GDC	61	63	64	58	59	60	61

Overall, concerning the physicochemical properties of the oxidized powders, XRF analysis revealed that the wt.% concentration of each dopant was close to the nominal, whereas XRD verified the detection of iron in the form of syn-Fe_2O_3 and gold as metallic Au. After H_2-reduction, there was formation of Ni-Fe, Ni-Au, Ni-Fe-Au, and Ni-Mo-Au solid solutions.

4. Catalytic—Kinetic Measurements

4.1. Carbon Deposition from the Catalytic CH_4 Dissociation Reaction—TGA Measurements

The carbon tolerance of the modified samples was studied isothermally at 800 °C by means of thermogravimetric (TG) analysis under 10 vol.% CH_4/Ar flow. The TG profiles (Figure 3) depict the change in weight (Δwt.%), as a function of time due to carbon deposition.

Specifically, the presented TG measurements investigated the activity of the examined samples for the catalytic CH_4 dissociation reaction and the concomitant carbon formation/deposition. In this reaction scheme, CH_4 is adsorbed and dissociates on the Ni surface sites (*) towards adsorbed H* and CH_x species, according to Equations (12)–(16) [4,52].

$$CH_4 + 2^* \leftrightarrow CH_3^* + H^* \quad (12)$$

$$CH_4 + ^* \leftrightarrow CH_4^* \quad (13)$$

$$CH_3^* + ^* \leftrightarrow CH_2^* + H^* \quad (14)$$

$$CH_2^* + ^* \leftrightarrow CH^* + H^* \quad (15)$$

$$CH^* + ^* \leftrightarrow C^* + H^* \quad (16)$$

The resulting adsorbed carbon (C*) species cover the surface of Ni, with subsequent diffusion and coverage of the bulk phase. The basic remark in this scheme is that the strongest CH_4 interaction with the Ni sites results in a higher carbon formation/deposition rate.

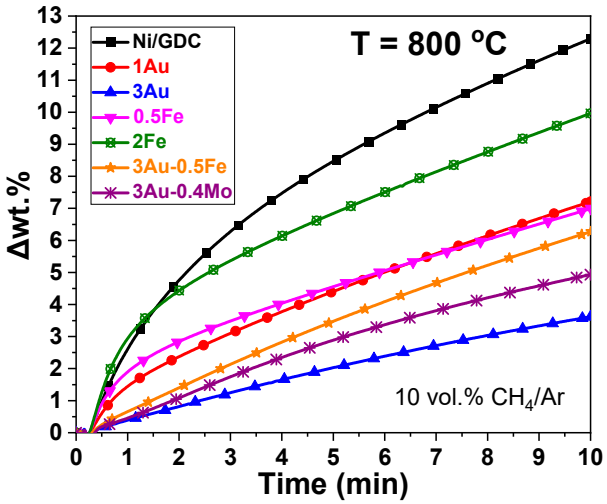

Figure 3. TG isothermal analysis of Mo-Au-Fe-Ni/GDC powders under 10 vol.% CH_4 in Ar at 800 °C. F_{tot} = 100 cm^3 min^{-1}.

The TG profiles (Figure 3) show that the modified samples exhibited lower activity for the catalytic CH_4 decomposition, and as a result sufficient tolerance to carbon formation/deposition when compared to Ni/GDC. Concerning the iron-modified samples, 2Fe-Ni/GDC and to a lesser extent 0.5Fe-Ni/GDC exhibited immediate and rapid weight increase due to carbon deposition, whereas after the first minute the wt.% increase was less acute. After 10 min under 10 vol.% CH_4/Ar exposure, the Fe-modified samples exhibited a slightly higher tolerance against coking than Ni/GDC. On the other hand, modification of Ni/GDC with 3 wt.% Au resulted in the highest carbon resistance when compared to the other samples. In regards to the ternary samples 0.5Fe-3Au-Ni/GDC and 0.4Mo-3Au-Ni/GDC, they exhibited adequate tolerance against carbon formation. Thus, the presence of 3 wt.% Au, with or without Fe/Mo, makes Ni/GDC less prone to carbon deposition.

The presented TGA results on Au and Mo-Au-Ni/GDC samples confirm previous findings from our research group [33]. Moreover, studies in the literature verify that Au can modify the catalytic activity of a Ni-based catalyst by inhibiting the dissociative adsorption of CH_4 or at least the dehydrogenation reaction steps that lead to carbon formation (Equations (12)–(16)) [52,53]. In particular, Fan et al. [53] employed DFT calculations to study the synergistic interaction between Ni and transition metal atoms (M = Cu, Ru, Rh, Pd, Ag, Pt, and Au) on M/Ni (1 1 1) surface alloys for CH_4 dissociation. In accordance with our results, it was found that the binding strength of CH_x was lower over Au-Ni (1 1 1) compared to Ni_3 sites. Additionally, the adsorption energy of C on Ni-Au sites was found to be less negative than that on the Ni (1 1 1) surface, indicating the inhibition of coke formation over Au/Ni catalysts.

4.2. Catalytic—Kinetic Investigation for the Dry CH_4 Reforming Reaction

Catalytic experiments at OCP mode on electrolyte-supported half cells were performed in order to have a reference on the performance and carbon tolerance of each electrocatalyst under CO_2 reforming of CH_4 reaction conditions, without the effect of the applied current (and consequently of the O^{2-} flux). Regarding the homogenous catalytic reaction, no activity was observed. In addition, since the specific measurements are going to be used as a reference catalytic profile for further full cell electrocatalytic measurements, it was decided to examine the effect of the applied current collector for the fuel electrode. In this respect, comparative measurements of Ni/GDC with and without the presence of Ni mesh (Figure S2 in the Supplementary Materials) showed that there is no direct catalytic contribution of the Ni mesh on the electrocatalysts' activity.

Figures 4 and 5 show the catalytic performance of each sample for the CO_2 reforming of CH_4 at 750–900 °C (CH_4/CO_2 = 50/50, $F_{tot,in}$ = 150 cm^3 min^{-1}). Specifically, Figure 4

depicts the consumption/production rates of CH_4, CO_2, H_2, CO, H_2O, and the formed carbon, whereas Figure 5 shows the % conversions of CH_4 and CO_2. The measurements were performed on electrolyte supported (half) cells that comprised only the fuel electrocatalyst and Ni mesh.

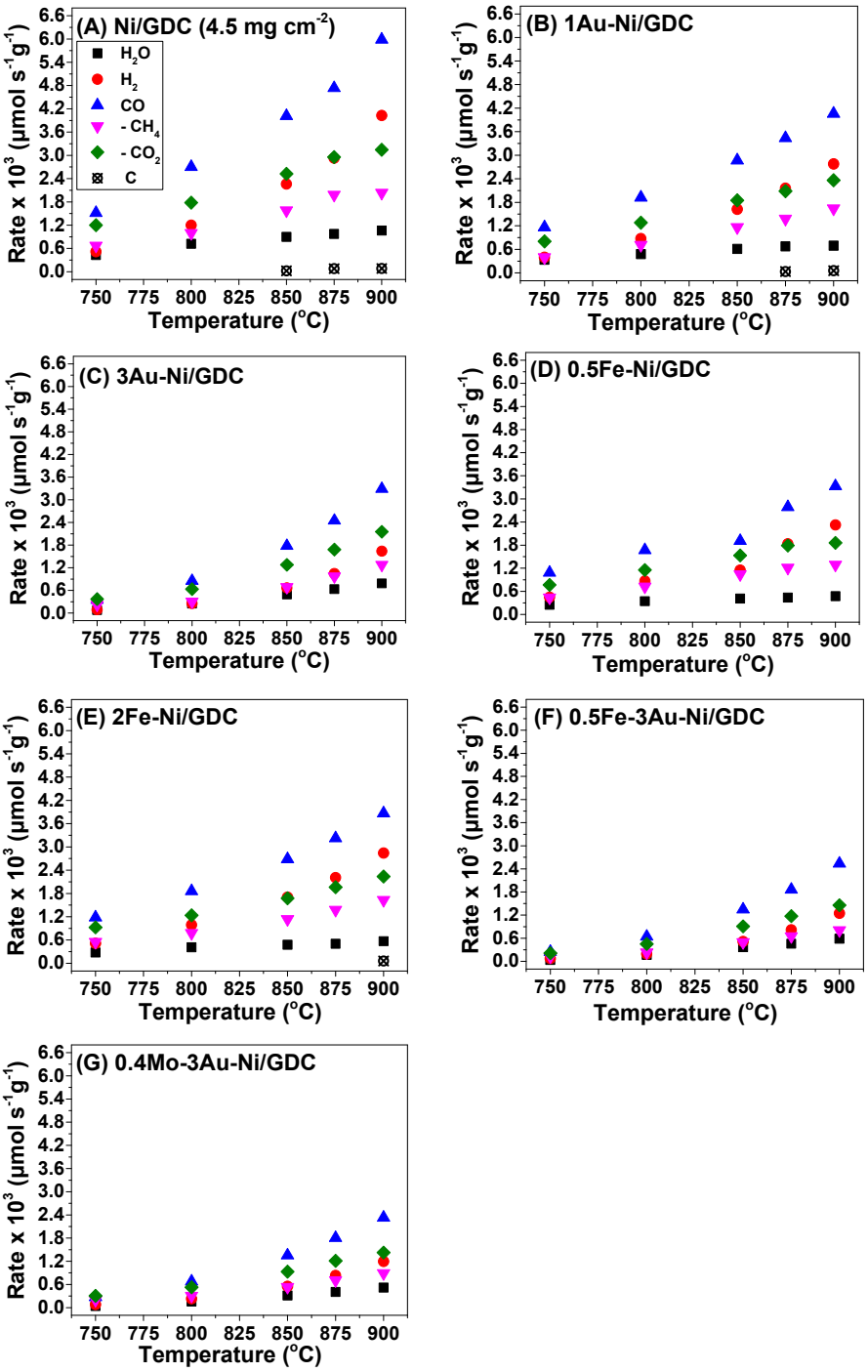

Figure 4. Production and consumption rates (µmol s^{-1} g^{-1}) of (**A**) Ni/GDC [54], (**B**) 1Au-Ni/GDC, (**C**) 3Au-Ni/GDC, (**D**) 0.5Fe-Ni/GDC, (**E**) 2Fe-Ni/GDC, (**F**) 0.5Fe-3Au-Ni/GDC [54], and (**G**) 0.4Mo-3Au-Ni/GDC [54] half cells at 750–900 °C. The reaction mixture comprised 50 vol.% CH_4 and 50 vol.% CO_2. F_{total} = 150 cm^3/min. Mass of each electrode ~6 mg/cm^2. OCP conditions. Data from (**A**,**F**,**G**) are reprinted from Ref. [54]. 2023, © The Electrochemical Society. Reproduced by permission of IOP Publishing Ltd. All rights reserved.

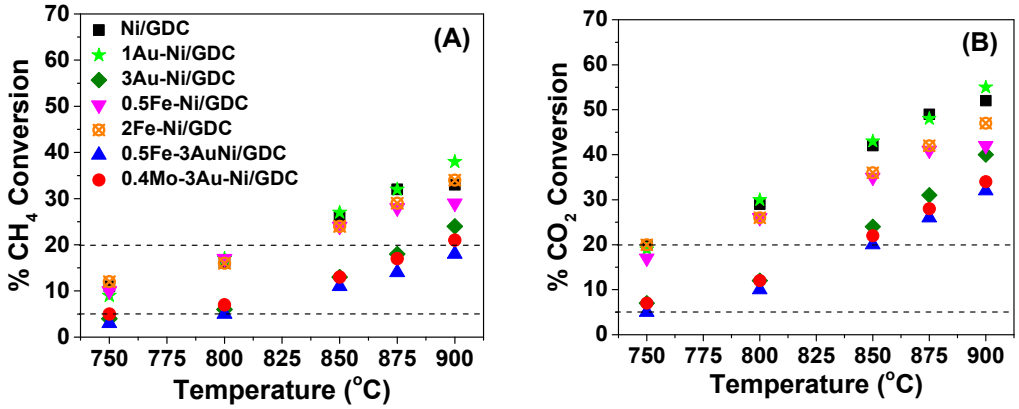

Figure 5. % Conversion of (**A**) CH_4 and (**B**) CO_2 for Ni/GDC, 1Au-Ni/GDC, 3Au-Ni/GDC, 0.5Fe-Ni/GDC, 2Fe-Ni/GDC, 0.5Fe-3Au-Ni/GDC, and 0.4Mo-3Au-Ni/GDC half cells at 750–900 °C. Reaction mixture = 50 vol.% CH_4−50 vol.% CO_2. F_{total} = 150 cm^3/min. Mass of each electrode = ~6 mg/cm^2. OCP conditions. The dashed lines correspond to the differential conditions region, where the CH_4 and CO_2 conversions varied in the region 5–20%.

In respect to the catalytic activity of Ni/GDC, it was found to be the most active sample for the CO_2 reforming of CH_4, yielding the highest consumption/production rates (Figure 4) and % conversions (Figure 5). However, it also exhibited measurable carbon formation rates at high temperatures (≥850 °C). The modified electrocatalysts were less active in terms of H_2 and CO production, but at the same time they were less prone to carbon formation (Figure 4). In particular, the majority of them did not show measurable carbon rates within the examined temperature region.

More specifically, 1Au-Ni/GDC and 2Fe-Ni/GDC were less active than Ni/GDC, but more active compared to the other modified samples (Figure 4). However, carbon formation was measured for both of these electrocatalysts at temperatures higher than 875 °C (Figure 4), which is a drawback for their use as potential fuel electrodes for the IDRM process. Although the above samples exhibited adequate tolerance to carbon formation under the catalytic decomposition of 10 vol.% CH_4/Ar at 800 °C (Figure 3), this did not apply for the DRM catalytic measurements under 50 vol.% CH_4−50 vol.% CO_2 (Figure 4). Furthermore, the fact that 1Au-Ni/GDC was prone to carbon formation (Figure 4) suggests that the 1 wt.% content of Au is probably too low to inhibit the coke formation under DRM reaction conditions.

On the other hand, 3Au-Ni/GDC and 0.5Fe-Ni/GDC showed sufficient carbon tolerance, but slightly lower rates than 1Au-Ni/GDC and 2Fe-Ni/GDC (Figure 4). Thus, it seems that the modification of Ni/GDC with 3 wt.% Au or 0.5 wt.% Fe inhibits carbon formation under DRM conditions and this observation concurs with the results from the TG analysis (Figure 3). Finally, the ternary samples 0.5Fe-3Au-Ni/GDC and 0.4Mo-3Au-Ni/GDC exhibited the lowest catalytic activity (Figure 4), but at the same time zero carbon deposits, which is also in agreement with the TGA results (Figure 3).

Regarding the % conversions of CO_2 and CH_4 at 750–900 °C (Figure 5), a general observation is that these values were lower than the thermodynamic equilibrium values at the corresponding temperatures under a mixture of CH_4/CO_2 = 1 at 1 atm (Table 4).

In addition, the % conversion of CO_2 at each temperature was always higher than the % conversion of CH_4. This is ascribed to the contribution of the RWGS reaction, which consumes CO_2 and H_2, resulting in a H_2/CO ratio less than unity [55–59]. Finally, the % conversions (Figure 5) and the consumption/production rates (Figure 4) increased by increasing the reaction temperature, due to the endothermic character of the DRM reaction [56,60].

Table 4. Equilibrium % conversions of CH_4 and CO_2 for stoichiometric carbon dioxide reforming of methane (at 1 atm) as a function of temperature [60,61].

Temperature (°C)	% CH_4	% CO_2
750	89.5	93.5
800	95.0	97.3
850	96.7	98.3
875	97.5	98.8
900	98.3	99.2

The "used" electrocatalysts, after the applied DRM conditions, were examined by means of scanning electron microscopy (SEM) with a HR − SEM (Zeiss SUPRA 35VP) (Figure S4 in the Supplementary Materials). Further analysis of the SEM images with the Gwyddion 2.49 software enabled the calculation of the particle size (Table S2 in the Supplementary Materials). As a general remark, the observed particles consist of both Ni and GDC and the mean diameter of their size was calculated in the range of 200 nm (std. error ± 10 nm), indicating similar agglomeration after the DRM measurement. Moreover, 0.5Fe-3Au-Ni/GDC and 0.4Mo-3Au-Ni/GDC exhibited larger "void space" when compared to Ni/GDC which is an indication of larger macro-porosity/tortuosity [35].

According to the literature [4,32,33,53,61–63], Au-Ni surface alloys exhibit less activity for methane reforming, but stronger resistance to carbon formation, even with small amounts of Au doping. Indicatively, DFT studies from Besenbacher et al. [62] on Au-Ni catalysts led to the suggestion that Au-Ni is less active in methane reforming, but more stable because the effect of Au on the atomic carbon adsorption was found to be stronger than on CH_4 activation. The low catalytic activity of Au-Ni-based catalysts is in accordance with the d-band center theory that was proposed by Nørskov et al. [62,63] dealing with the dissociation of CH_4 on the Ni surface doped with Au. According to these studies, the rate of CH_4 dissociation and consequently the amount of carbon formation (Equations (12)–(16)) can be inhibited on Au-modified surfaces, due to the fact that the center of the d-band density of states is displaced to lower energies below the Fermi level of Ni. The same trend can be considered for the case where Au, Mo, and Ni coexist through the formation of the ternary solid solution [33]. The latter remark has been confirmed in previous studies [32–34] for the catalytic and electrocatalytic internal H_2O reforming of CH_4 (also in the presence of 10 ppm H_2S) where the 0.4Mo-3Au-Ni/GDC electrode was the least prone to carbon deposition (and sulfur poisoning) and the most active electrocatalytically, compared to both the non-doped and the Au-doped electrodes.

Other studies proposed that carbon formation in reforming processes depends on the size of metal particles [64,65]. Thus, smaller Ni particles have stronger ability to inhibit coke deposition, suggesting high stability of the catalytic activity [66]. In the present study, the particle size of Ni was smaller in all modified samples compared to Ni/GDC. Another remark especially for the case of the CO_2 reforming of CH_4 is that the addition of a small amount of a noble metal (i.e., Au in our case) favors CO_2 dissociation, resulting in oxygen formation that can assist the coke removal from the catalyst surface [4].

Furthermore, in regards to the Fe-Ni surface alloys/solid solutions, these have been proposed to partially promote carbon gasification [39–43,67]. Specifically, S.M. Kim et al. reported [67] that Fe in Ni-Fe alloys is partially oxidized by CO_2 to FeO ($CO_2 + Fe \rightarrow CO + FeO$), which in turn provides lattice oxygen to the deposited carbon on the surface, leading to its partial oxidation to CO ($C + FeO \rightarrow CO + Fe$), and therefore results in materials with improved coke tolerance. In the present study, only the 0.5Fe-Ni/GDC sample was found to be tolerant towards coke formation, whereas 2Fe-Ni/GDC was prone to carbon deposition. Finally, the 0.5Fe-3Au-Ni/GDC is a new proposed electrocatalyst that combines the improved catalytic characteristics of Au and Fe towards elimination of carbon deposits, although it exhibited lower catalytic performance compared to Ni/GDC.

Therefore, in an attempt to further investigate the observed differences on the catalytic activity, kinetic measurements were performed by applying fuel reaction inlet flows in the

range of 150–300 cm^3/min. The objective of the applied flows was to keep the CH_4 and CO_2 conversions in the region between 5–20%, thus assuring operation under differential conditions. It should be noted that in the above fuel inlet range the reaction rates were found to remain practically constant, which indicates the absence of mass transfer limitations.

Specifically, Ni/GDC was the most catalytically active sample, yielding high % CH_4 and CO_2 conversions that were beyond the differential conditions region. In order to achieve this experimental parameter, it was necessary to decrease the mass loading of the sample from 5 mg/cm^2 to 2.5 mg/cm^2 and to perform a new series of kinetic measurements (Figure S3 in the Supplementary Materials). Similarly, in the case of the modified samples, the F_{total} was fixed in the range of 150–300 cm^3/min with a mass loading of ~6 mg/cm^2 (Table S1 in the Supplementary Materials). In addition, for reliable comparison reasons, a Ni/GDC electrode with a similar loading (5 mg/cm^2) as the modified samples was studied kinetically in the range of 250–300 cm^3/min (Table S1 in the Supplementary Materials).

Figure 6 presents the Arrhenius plots for the production rates of CO, H_2, and H_2O and the consumption rates of CH_4 and CO_2 and Table 5 presents the calculated apparent activation energies ($E_{a,app}$) for each electrocatalyst under differential conditions. The $E_{a,\,app}$ for the production of H_2O (Figure 6C) corresponds to the apparent activation energy for the RWGS reaction, which consumes the valuable H_2 for the fuel cell and is considered as a non-desired side reaction for the SOFC IDRM process. Modification of Ni/GDC with iron seems to favor the RWGS reaction, since $E_{a,app}$ values of 0.5Fe-Ni/GDC and 2Fe-Ni/GDC were quite low for H_2O production. The same observation also applies for the 1Au-Ni/GDC electrode. Moreover, the above samples exhibited quite similar $E_{a,app}$ values like Ni/GDC for CH_4 and CO_2 consumption. Concerning H_2 and CO production, 0.5Fe-Ni/GDC, 1Au-Ni/GDC, and mainly 2Fe-Ni/GDC exhibited lower $E_{a,app}$ values than that of Ni/GDC.

Table 5. Apparent Activation Energies ($E_{a,app}$, kJ mol^{-1}) of modified electrodes under differential conditions for H_2O, H_2, and CO production and CH_4, CO_2 consumption derived from Figure 6 and calculated from the Arrhenius equation.

Sample	$E_{a,app}$ * (kJ mol^{-1}) per Product or Reactant				
	H_2O	**H_2**	**CO**	**CH_4**	**CO_2**
Ni/GDC_1*	139	167	125	64	85
Ni/GDC_2*	142	147	126	63	73
1Au	108	146	112	67	78
3Au	179	184	157	95	113
0.5Fe	104	143	107	71	76
2Fe	102	108	93	72	79
0.5Fe-3Au	204	193	167	138	146
0.4Mo-3Au	191	178	154	88	105

: Arrhenius eq. $r = A \exp(-\frac{E_{a,app}}{R \cdot T})$. Ni/GDC with a mass of 1: 2.5 mg cm^{-2} and 2*: 5 mg cm^{-2}.

On the other hand, modification of Ni/GDC with 3 wt.% Au seems to hinder the activity for the RWGS reaction, since the $E_{a,app}$ values of 3Au-Ni/GDC, 0.5Fe-3Au-Ni/GDC, and 0.4Mo-3Au-Ni/GDC were higher than those of the other examined samples. In addition, the specific electrocatalysts were less prone to carbon formation and less active for H_2 and CO production with relatively high $E_{a,app}$ values when compared to Ni/GDC and the Fe-modified electrodes. Finally, the fact that 2Fe-Ni/GDC and Ni/GDC were the samples where carbon formation was detected is a point that needs to be also taken into account.

According to the literature, CH_4 decomposition (Equation (12)) is the rate-determining step at high temperatures for both DRM and decomposition reactions [65,68,69]. Experimental kinetic studies [68,70] coincide with theoretical studies [65,69] for the reaction mechanism, which suggests that CH_4 decomposition demands higher energy than further decomposition of CH_x ($x \leq 3$) (Equations (14)–(16)). Thus, the available research data focus on activation energy values for CH_4 activation/consumption. Moreover, it is generally

accepted that CH_4 is decomposed on metal surface sites (e.g., Ni), whereas CO_2 is mainly activated on support sites (e.g., GDC in the case of the examined electrocatalysts) on the vicinity of dispersed metal particles or/and on the metallic sites [4,52]. As reported in the literature, the calculated activation energies for Ni-based catalysts in the DRM process vary within a wide range between 29 and 360 kJ/mol, which depends on the nature of the support, the presence of additives, and the catalytic conditions [58,70,71]. The most frequently reported $E_{a,app}$ value for Ni-based catalysts is ~60 kJ/mol, which concurs with our calculated $E_{a,app}$ for Ni/GDC and coincides with the $E_{a,app}$ for CH_4 dissociation on Ni (1 1 0) and Ni (1 1 1) [72]. It should be noted that very low $E_{a,app}$ values may reflect mass transfer limitation phenomena [72,73].

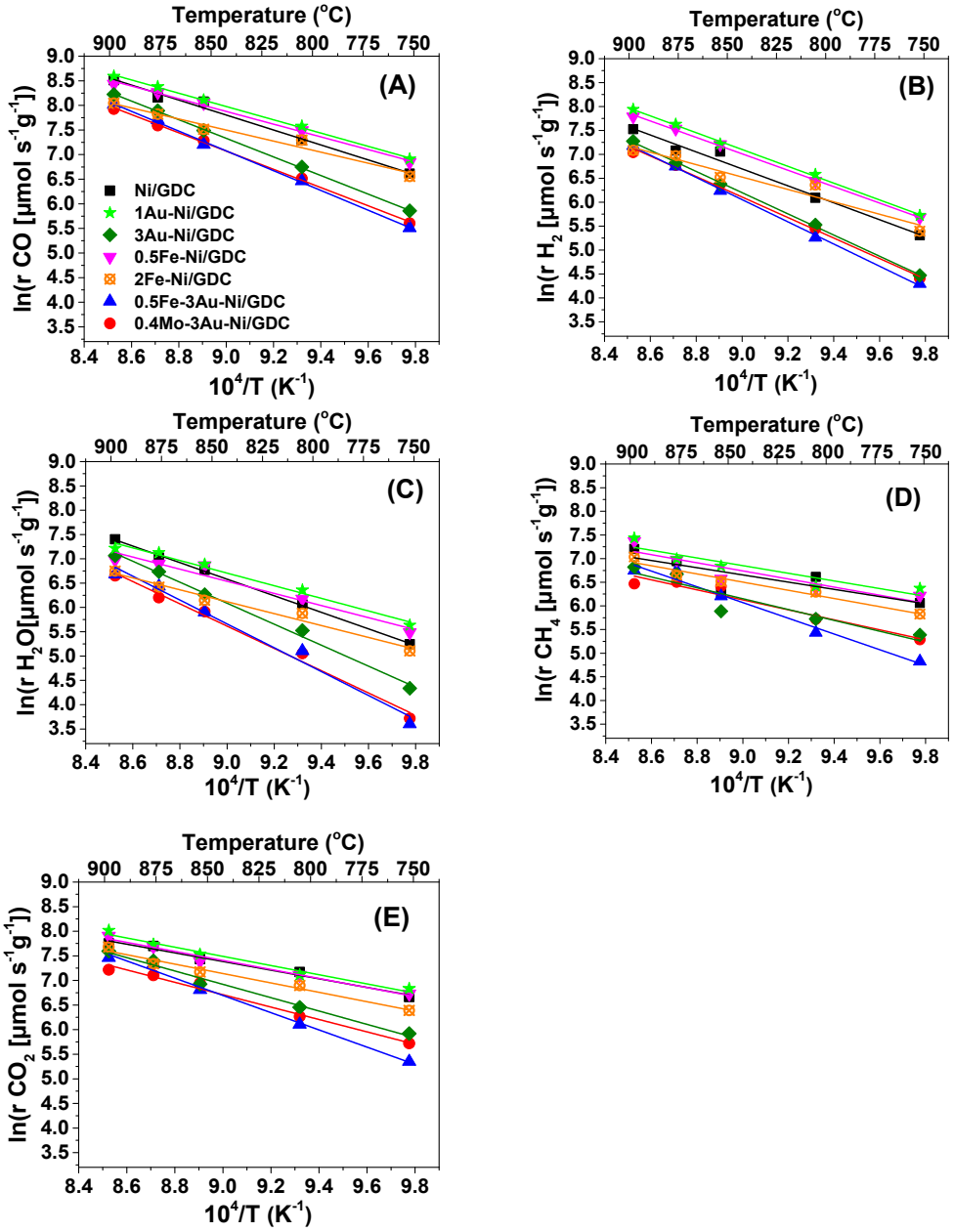

Figure 6. Arrhenius plots of the inherent production of (**A**) CO, (**B**) H_2, and (**C**) H_2O and consumption of (**D**) CH_4 and (**E**) CO_2 as a function of temperature (750–900 °C). Differential conditions (Conversions: 5–20%) under the reaction mixture of 50 vol.% CH_4 − 50 vol.% CO_2. F_{total} (cm^3 min^{-1}) and mass (mg cm^{-2}) of each half cell as a function of temperature (750–900 °C) is depicted in Table S1 in the Supplementary Materials.

The modification of Ni/GDC with 3 wt.% Au and 0.4 wt.% Mo-3 wt.% Au, as well as with 0.5 wt.% Fe-3 wt.% Au, increased the $E_{a,app}$ for CH_4 dissociation, suggesting that the catalytic activity of the surface Ni active sites has been inhibited for this reaction. Furthermore, the fact that Ni-Au modification increased the $E_{a,app}$ for CH_4 reforming reactions has been also observed in other studies [62,74]. Overall concerning the selection of the proper electrocatalyst for the IDRM reaction, it is suggested that this should exhibit (a) the lowest $E_{a,app}$ for H_2 and CO production, (b) the highest $E_{a,app}$ for H_2O production, and (c) negligible carbon formation rates.

The kinetic investigation dealt also with the dependency of the H_2, CO, and H_2O production rates on various CH_4 and CO_2 molar fractions (y_{CH4}, y_{CO2}). These measurements also took place under differential conditions, by varying the applied gas flows between 150 and 300 cm^3/min. The examined electrocatalysts (in the form of half cells) were Ni/GDC and 0.4Mo-3Au-Ni/GDC with mass loadings of 2.5 and 7.5 mg/cm^2, respectively. The effect of y_{CH4} and y_{CO2} on the production rates for Ni/GDC is shown in Figures 7 and 8, whereas for 0.4Mo-3Au-Ni/GDC it is shown in Figures 9 and 10.

Concerning Ni/GDC, it is observed that the production rates of H_2 and CO exhibited a positive order dependence either on y_{CH4} (Figure 7A,B) or on y_{CO2} (Figure 8A,B) at 850 and 900 °C. On the other hand, the production rate of H_2O showed an initially positive and then zero order dependence on y_{CH4} (Figure 7C), whereas it was positive on y_{CO2} (Figure 8C) at the same temperatures (850 and 900 °C). At 750 °C the general remark is the inhibition of the catalytic activity towards the production of H_2, CO, and H_2O. Moreover, at each temperature and fuel feed, the CO production rates were higher than that of H_2, due to the fact that CO is produced both through the DRM (Equation (1)) and the RWGS (Equation (2)) reactions.

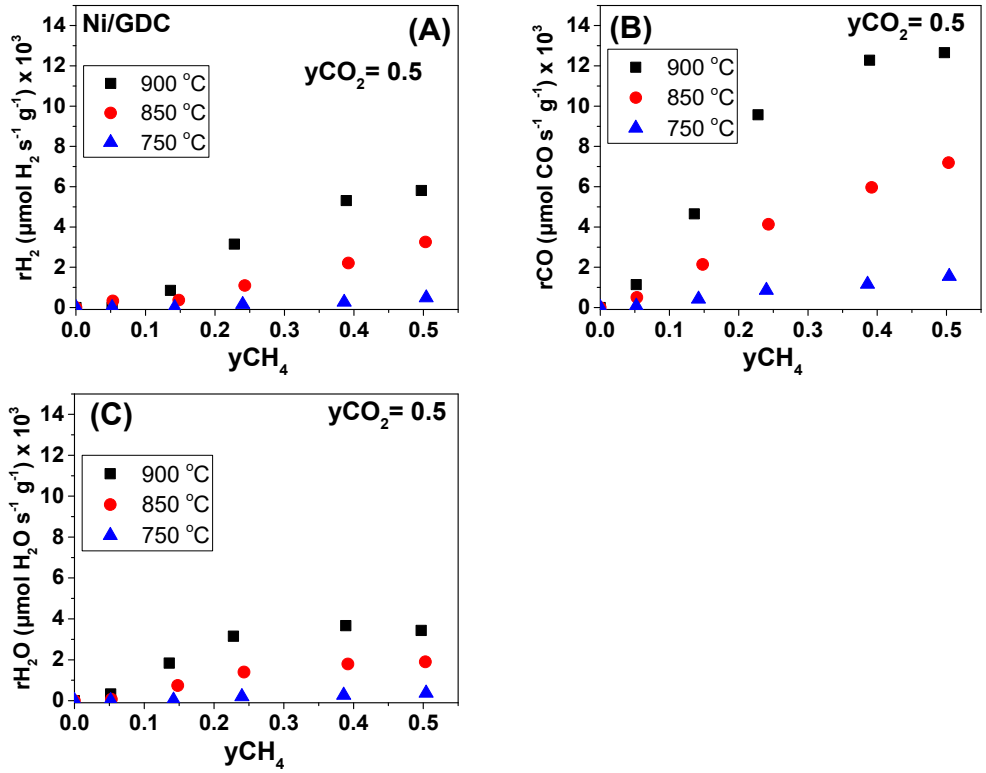

Figure 7. Steady-state effect of CH_4 molar fraction (y_{CH4}) under fixed CO_2 molar fraction (y_{CO2} = 0.5) on the (**A**) H_2 production rate, (**B**) CO production rate, and (**C**) H_2O production rate under OCP conditions. Half-cell with Ni/GDC (2.5 mg/cm^2). Differential conditions (Conversions: 5–20%).

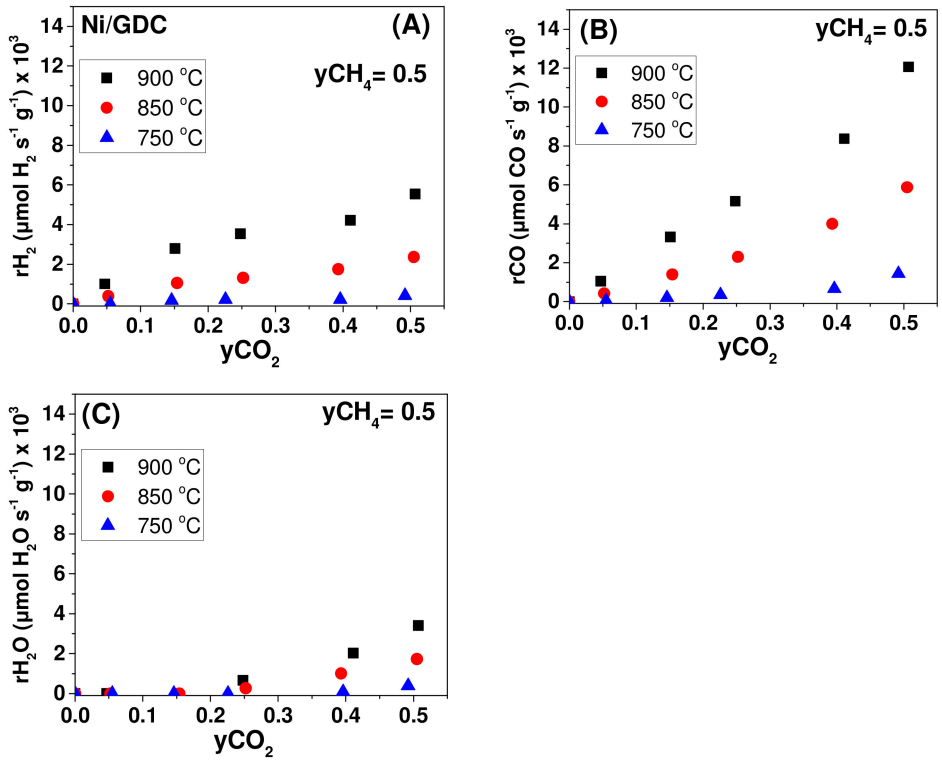

Figure 8. Steady-state effect of CO_2 molar fraction (y_{CO2}) under fixed CH_4 molar fraction (y_{CH4} = 0.5) on the (**A**) H_2 production rate, (**B**) CO production rate, and (**C**) H_2O production rate under OCP conditions. Half-cell with Ni/GDC (2.5 mg/cm^2). Differential conditions (Conversions: 5–20%).

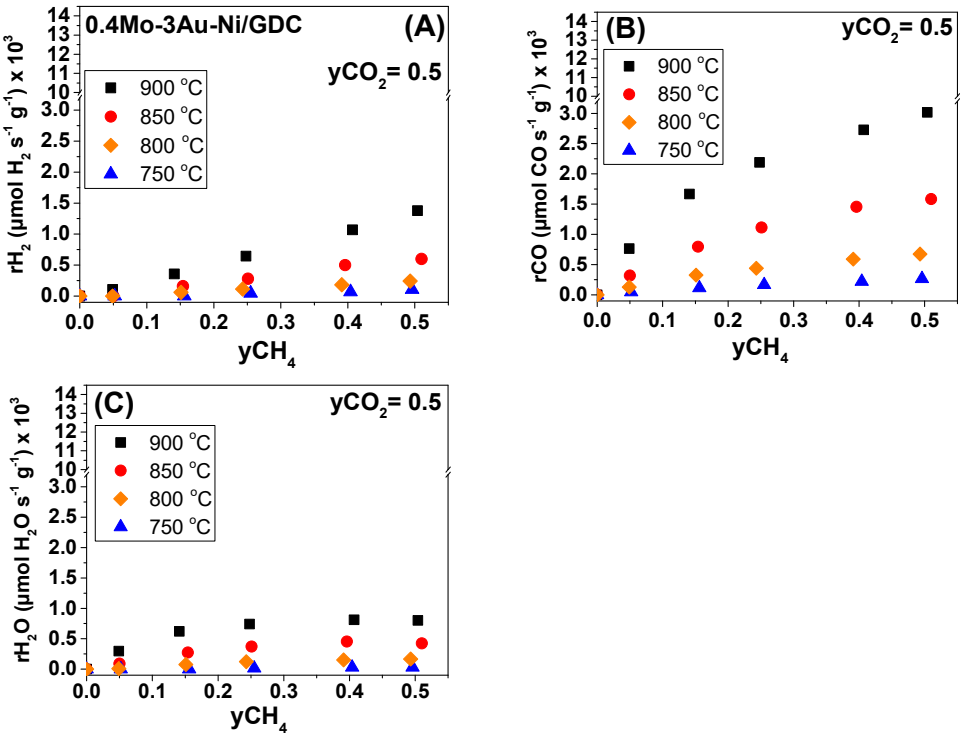

Figure 9. Steady-state effect of CH_4 molar fraction (y_{CH4}) under fixed CO_2 molar fraction (y_{CO2} = 0.5) on the (**A**) H_2 production rate, (**B**) CO production rate, and (**C**) H_2O production rate under OCP conditions. Half-cell with 0.4Mo-3Au-Ni/GDC (7.5 mg/cm^2). Differential conditions (Conversions: 5–20%).

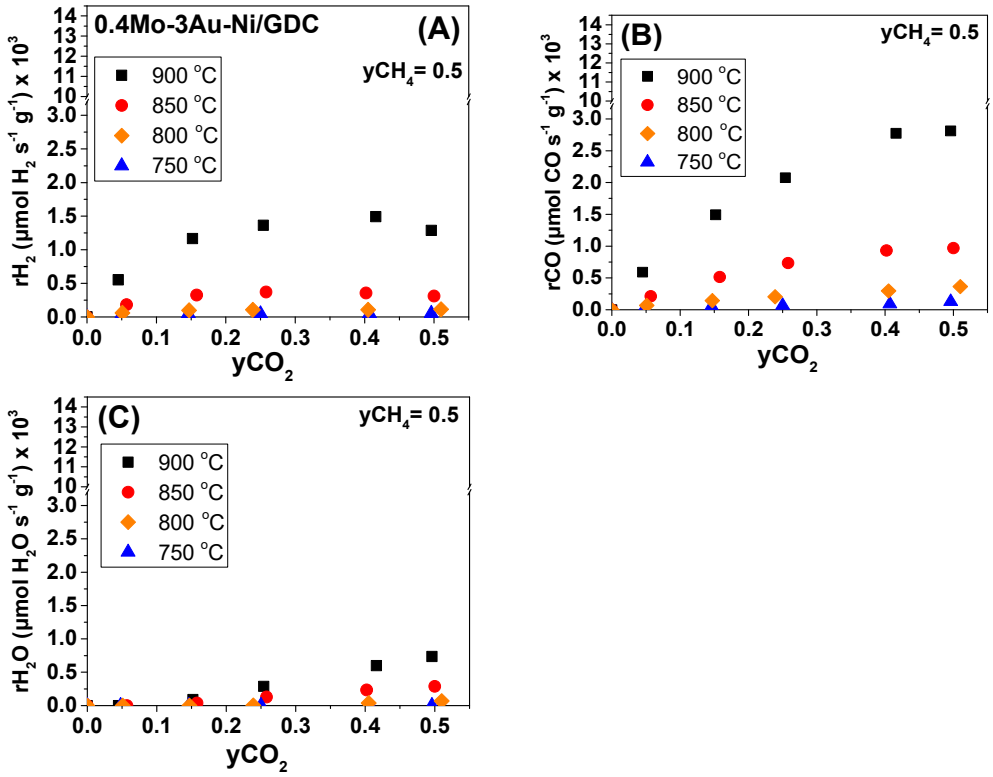

Figure 10. Steady-state effect of CO_2 molar fraction (y_{CO2}) under fixed CH_4 molar fraction (y_{CH4} = 0.5) on the (**A**) H_2 production rate, (**B**) CO production rate, and (**C**) H_2O production rate under OCP conditions. Half-cell with 0.4Mo-3Au-Ni/GDC (7.5 mg/cm^2). Differential conditions (Conversions: 5–20%).

Interestingly, at the high temperature of 900 °C the production rates of H_2, CO, and H_2O approached a maximum at $y_{CH4} \geq 0.4$ by keeping constant y_{CO2} = 0.5 (Figure 7). On the contrary, at the same temperature, r_{H2}, r_{CO}, and r_{H2O} increased within the whole y_{CO2} range, while y_{CH4} = 0.5 (Figure 8). The positive reaction order of the production rates versus y_{CH4} and y_{CO2} and the appearance of a maximum at $y_{CH4} \geq 0.4$ at 900 °C indicate that most probably the dissociative adsorption of CH_4 can be the limiting step of the DRM reaction on Ni/GDC, which is in agreement with other studies [65,68–70]. Finally, it should be noted that under low y_{CO2} (<0.25) (Figure 8C) the production of H_2O, through the RWGS reaction, was negligible and as a result the produced CO is derived solely from the DRM reaction. In this case and in the region of $y_{CO2} < 0.25$, the produced r_{H2} should be identical with the produced r_{CO}, which was confirmed (Figure 8A,B).

In regards to the 0.4Mo-3Au-Ni/GDC sample at T < 800 °C (i.e., 750 °C), the overall catalytic activity was inhibited, similar to Ni/GDC. At ≥ 800 °C, a positive order dependence was also observed for the production rates of H_2 and CO by varying y_{CH4} (Figure 9A,B). However, by varying the y_{CO2} and at temperatures > 800 °C (Figure 10A,B), the trend of r_{H2} and r_{CO} was different when compared to Ni/GDC. Specifically, in the non-modified sample the production rate of H_2 and CO increased within the whole range of the applied y_{CO2}, while y_{CH4} = 0.5 (Figure 8A,B). On the other hand, in the case of the Mo-Au-modified sample, at T ≥ 800 °C the r_{H2} and r_{CO} reached to a maximum for $y_{CO2} \geq 0.25$ (Figure 10A,B). This maximum indicates that the DRM reaction mechanism for 0.4Mo-3Au-Ni/GDC might be different when compared to Ni/GDC. In particular, it can be suggested that on the active sites of the Mo-Au-Ni-modified electrocatalyst there is a point where the dissociative adsorption of CO_2 reached faster to equilibrium and to a stable surface coverage. As a result, the production of CO and H_2 did not increase any further by increasing the y_{CO2} when compared to Ni/GDC.

Concerning the production rate of H_2O on the 0.4Mo-3Au-Ni/GDC, it exhibited the same trend like on the non-modified sample. Specifically, r_{H2O} initially showed a positive

order dependence on y_{CH4} (Figure 9C), which altered to zero at $y_{CH4} \geq 0.25$. Moreover, the dependence of r_{H2O} on the applied y_{CO2} (Figure 10C) was positive.

Therefore, the observation that in the presented DRM reactions scheme H_2O is produced only through the RWGS reaction, in combination with the similar dependence of r_{H2O} on y_{CH4} and y_{CO2}, suggest that both of the Ni/GDC and 0.4Mo-3Au-Ni/GDC electrocatalysts perform the RWGS reaction through the same mechanism. On the other hand, by considering that CO is produced both through DRM and RWGS, it can be assumed that the mechanism of the main DRM reaction may be different for 0.4Mo-3Au-Ni/GDC than that of Ni/GDC, which is a remark that needs to be further studied. Furthermore, the calculated $E_{a,app}$ from the Arrhenius plots and the formation rates of carbon highlight that the modified 3Au-Ni/GDC, 0.5Fe-3Au-Ni/GDC, and 0.4Mo-3Au-Ni/GDC samples exhibited (i) the highest $E_{a,app}$ for the non-desired RWGS reaction, (ii) high tolerance to carbon formation, and (iii) they were less active for H_2 and CO production, as well as for the CH_4 decomposition. Therefore, and for the purposes of a following separate manuscript, there will be selection among these three samples for electro-catalytic measurements and comparison with the SoA Ni/GDC in the form of full cells for the internal DRM process.

5. Conclusions

The present study dealt with the physicochemical and kinetic investigation of Fe, Au, Fe-Au, and Mo-Au modified Ni/GDC electrocatalysts towards their performance for the DRM, RWGS, and CH_4 decomposition reactions, as well as their tolerance to carbon formation. The research objective of this investigation focuses on the sustainable conversion of the greenhouse CH_4 and CO_2 gases towards syngas by means of Solid Oxide Fuel cells, which is a highly efficient and environmentally friendly electrochemical source of energy/power and useful chemicals. In this respect, the catalytic-kinetic investigation, in combination with the detailed physicochemical characterization, of a variety of new candidate fuel electrodes is the first key step to understand the underlying catalytic profile and to elucidate the occurring reactions during the IDRM process.

Regarding the physicochemical properties of the oxidized powders, XRF analysis revealed that the wt.% concentration of each dopant was close to the nominal, whereas XRD verified the detection of iron in the form of syn-Fe_2O_3 and gold as metallic Au. After H_2-reduction, there was formation of Ni-Fe, Ni-Au, Ni-Fe-Au, and Ni-Mo-Au solid solutions. TG analysis at 800 °C, under 10 vol.% CH_4/Ar, showed that the modified samples exhibited lower activity for the catalytic CH_4 decomposition and were less prone to carbon deposition when compared to Ni/GDC. Specifically, modification with 3 wt.% Au, with or without Fe/Mo, resulted in the highest carbon tolerance.

In respect to the catalytic performance of electrolyte-supported half cells, Ni/GDC was found to be the most active sample for the CO_2 reforming of CH_4. However, it exhibited carbon formation rates at high temperatures ($\geq$850 °C). On the other hand, 3Au-Ni/GDC, 0.5Fe-Ni/GDC, 0.5Fe-3Au-Ni/GDC, and 0.4Mo-3Au-Ni/GDC were less active catalytically, but at the same time exhibited higher tolerance to carbon deposition. Concerning the selection of the proper electrocatalyst for the IDRM reaction, it is suggested that this should preferably exhibit (a) the lowest $E_{a,app}$ for H_2 and CO production, (b) the highest $E_{a,app}$ for H_2O production which results mainly from the RWGS and is considered as an undesired side reaction for the SOFC IDRM process, and (c) negligible carbon formation. These kinetic pre-conditions seem to be followed by the modified 3Au-Ni/GDC, 0.5Fe-3Au-Ni/GDC, and 0.4Mo-3Au-Ni/GDC electrocatalysts.

Further kinetic analysis on Ni/GDC and 0.4Mo-3Au-Ni/GDC showed similar dependence of r_{H2O} on y_{CH4} and y_{CO2}, suggesting that the RWGS side reaction may be performed through the same mechanism on both samples. On the other hand, it was observed that the mechanism of the main DRM reaction may be different for the 0.4Mo-3Au-Ni/GDC when compared to Ni/GDC. This is because the Mo-Au-modified sample (i) was less active for the catalytic CH_4 decomposition reaction and thus less prone to carbon formation, and (ii)

at high temperature (≥800 °C) and constant y_{CH4} the dissociative adsorption of CO_2 seems to reach faster to a stable surface coverage when compared to Ni/GDC.

Overall, the present study is a thorough investigation on the development of modified Ni/GDC electrocatalysts with enhanced efficiency and carbon tolerance when compared to the SoA. The selected samples, namely 3Au-Ni/GDC, 0.5Fe-3Au-Ni/GDC, and 0.4Mo-3Au-Ni/GDC, meet the experimentally defined kinetic prerequisites for the SOFC IDRM reaction. Therefore, the reported findings are considered as a significant contribution for the practical application of this technology with a valuable impact in the research field of sustainable energy. These samples are currently under further investigation as electrodes for the purposes of a separate manuscript in full cell SOFC measurements and long-term stability operation.

Supplementary Materials: The following supporting information can be downloaded at https://www.mdpi.com/article/10.3390/en17010184/s1, Figure S1. XRD patterns of the oxidized [(A),(B),(C)] (calcined at 1100 °C) and [(D)] H_2-reduced (900 °C) powders. Furthermore, there are magnifications of the main XRD peaks for the oxidized (1100 °C) powders: (B) NiO (0 1 2) peak in the range of $42.8° \leq 2\theta \leq 43.6°$ and (C) GDC (2 2 2) peak in the range of $28.0° \leq 2\theta \leq 28.8°$. Figure S2. Catalytic investigation of a half cell with: (A), (C) Ni/GDC without Ni mesh and (B), (D) Ni/GDC with Ni mesh, at 750–900 °C, in terms of (A), (B) rate and (C), (D) % conversion. The reaction mixture comprised 50 vol.% CH_4 and 50 vol.% CO_2. OCP conditions. F_{total} = 150 cm^3/min. Mass of Ni/GDC electrode ~5 mg/cm^2. Figure S3. Catalytic investigation of Ni/GDC under differential conditions, in terms of (A) % conversion of CH_4 and CO_2, (B) production and consumption inherent rates (μmol s^{-1} g^{-1}) and (C) Arrhenius plots of the inherent rates as a function of temperature (750–900 °C). Reaction mixture: 50 vol.% CH_4−50 vol.% CO_2. F_{total} was 150 cm^3/min at 750–850 °C and 200 cm^3/min at 875 and 900 °C. Mass: 3 mg/cm^2. Figure S4. SEM of the surface side of the used Mo-Au-Fe-Ni/GDC half cells, after DRM catalytic study. Table S1: $F_{total,inlet}$ (cm^3 min^{-1}) per half cell, under differential conditions (Conversions: 5–20%) as a function of temperature (750–900 °C). Mass (mg cm^{-2}) of each cell is also depicted. Table S2: Mean diameter (nm) of 100 particles, per Mo-Au-Fe-Ni/GDC half cell, from Figure S4 after SEM analysis. Used cells after DRM study.

Author Contributions: Conceptualization, S.G.N. and D.K.N.; Methodology, E.I., S.G.N. and D.K.N.; Validation, E.I., S.G.N. and D.K.N.; Formal analysis, E.I.; Investigation, E.I.; Resources, D.K.N.; Data curation, E.I. and D.K.N.; Writing—original draft, E.I.; Writing—review & editing, E.I. and D.K.N.; Visualization, E.I. and D.K.N.; Supervision, S.G.N. and D.K.N.; Project administration, D.K.N.; Funding acquisition, S.G.N. and D.K.N. All authors have read and agreed to the published version of the manuscript.

Funding: The research leading to these results has received funding from the European Union and Greek national funds through the operational program 'Regional Excellence' and the operational program 'Competitiveness, Entrepreneurship, and Innovation', under the call "RESEARCH-CREATE-INNOVATE" (Project code: Eco-Bio-H2-FCs, T2EΔK-00955) and from the Fuel Cells and Hydrogen Two Joint Undertaking (now Clean Hydrogen Partnership) under the project 24_7 ZEN [Horizon Europe], Grant Agreement No. 101101418. This Joint Undertaking receives support from the European Union's Horizon 2020 Research and Innovation program, Hydrogen Europe and Hydrogen Europe Research.

Data Availability Statement: Data are contained within the article and Supplementary Materials.

Acknowledgments: The authors would like to thank Vayia Xanthopoulou, researcher at the Laboratory of Electron Microscopy and Microanalysis, School of Natural Sciences, University of Patras, for the XRF analysis.

Conflicts of Interest: The authors declare no conflict of interest.

References

1. Escudero, M.J.; Maffiotte, C.A.; Serrano, J.L. Long-term operation of a solid oxide fuel cell with MoNi–CeO_2 as anode directly fed by biogas containing simultaneously sulphur and siloxane. *J. Power Sources* **2021**, *481*, 229048. [CrossRef]
2. Yentekakis, I.V.; Dong, F. Grand Challenges for Catalytic Remediation in Environmental and Energy Applications toward a Cleaner and Sustainable Future. *Front. Environ. Chem.* **2020**, *1*, 5. [CrossRef]

3. Aramouni, N.A.K.; Touma, J.G.; Tarboush, B.A.; Zeaiter, J.; Ahmad, M.N. Catalyst design for dry reforming of methane: Analysis review. *Renew. Sustain. Energy Rev.* **2018**, *82*, 2570–2585. [CrossRef]
4. Yentekakis, I.V.; Panagiotopoulou, P.; Artemakis, G. A review of recent efforts to promote dry reforming of methane (DRM) to syngas production via bimetallic catalyst formulations. *Appl. Catal. B Environ.* **2021**, *296*, 120210. [CrossRef]
5. Niu, J.; Guo, F.; Ran, J.; Qi, W.; Yang, Z. Methane dry (CO_2) reforming to syngas (H_2/CO) in catalytic process: From experimental study and DFT calculations. *Int. J. Hydrogen Energy* **2020**, *45*, 30267–30287. [CrossRef]
6. Faro, M.L.; Vita, A.; Pino, L.; Aricò, A.S. Performance evaluation of a solid oxide fuel cell coupled to an external biogas tri-reforming process. *Fuel Process. Technol.* **2013**, *115*, 238–245. [CrossRef]
7. Chiodo, V.; Galvagno, A.; Lanzini, A.; Papurello, D.; Urbani, F.; Santarelli, M.; Freni, S. Biogas reforming process investigation for SOFC application. *Energy Convers. Manag.* **2015**, *98*, 252–258. [CrossRef]
8. Shiratori, Y.; Ijichi, T.; Oshima, T.; Sasaki, K. Internal reforming SOFC running on biogas. *Int. J. Hydrogen Energy* **2010**, *35*, 7905–7912. [CrossRef]
9. Sarno, C.; Luisetto, I.; Zurlo, F.; Licoccia, S.; Di Bartolomeo, E. Lanthanum chromite based composite anodes for dry reforming of methane. *Int. J. Hydrogen Energy* **2018**, *43*, 14742–14750. [CrossRef]
10. Papadam, T.; Goula, G.; Yentekakis, I.V. Long-term operation stability tests of intermediate and high temperature Ni-based anodes' SOFCs directly fueled with simulated biogas mixtures. *Int. J. Hydrogen Energy* **2012**, *37*, 16680–16685. [CrossRef]
11. Santoro, M.; Di Bartolomeo, E.; Luisetto, I.; Aricò, A.; Squadrito, G.; Zignani, S.; Faro, M.L. Insights on the electrochemical performance of indirect internal reforming of biogas into a solid oxide fuel cell. *Electrochim. Acta* **2022**, *409*, 139940. [CrossRef]
12. Saadabadi, S.A.; Thattai, A.T.; Fan, L.; Lindeboom, R.E.F.; Spanjers, H.; Aravind, P.V. Solid Oxide Fuel Cells fuelled with biogas: Potential and constraints. *Renew. Energy* **2019**, *134*, 194–214. [CrossRef]
13. Yentekakis, I.V.; Goula, G. Biogas management: Advanced utilization for production of renewable energy and added-value chemicals. *Front. Environ. Sci.* **2017**, *5*, 7. [CrossRef]
14. Sengodan, S.; Lan, R.; Humphreys, J.; Du, D.; Xu, W.; Wang, H.; Tao, S. Advances in reforming and partial oxidation of hydrocarbons for hydrogen production and fuel cell applications. *Renew. Sustain. Energy Rev.* **2018**, *82*, 761–780. [CrossRef]
15. Barelli, L.; Ottaviano, A. Solid oxide fuel cell technology coupled with methane dry reforming: A viable option for high efficiency plant with reduced CO_2 emissions. *Energy* **2014**, *71*, 118–129. [CrossRef]
16. Qiu, P.; Sun, S.; Yang, X.; Chen, F.; Xiong, C.; Jia, L.; Li, J. A review on anode on-cell catalyst reforming layer for direct methane solid oxide fuel cells. *Int. J. Hydrogen Energy* **2021**, *46*, 25208–25224. [CrossRef]
17. Gür, T.M. Comprehensive review of methane conversion in solid oxide fuel cells: Prospects for efficient electricity generation from natural gas. *Prog. Energy Combust. Sci.* **2016**, *54*, 1–64. [CrossRef]
18. Zhang, H.; Liu, W.; Wang, J.; Yang, J.; Chen, Y.; Guan, W.; Singhal, S.C. Power generation from a symmetric flat-tube solid oxide fuel cell using direct internal dry-reforming of methane. *J. Power Sources* **2021**, *516*, 230662. [CrossRef]
19. Abdelkareem, M.A.; Tanveer, W.H.; Sayed, E.T.; Assad, M.E.H.; Allagui, A.; Cha, S.W. On the technical challenges affecting the performance of direct internal reforming biogas solid oxide fuel cells. *Renew. Sustain. Energy Rev.* **2019**, *101*, 361–375. [CrossRef]
20. Pakhare, D.; Spivey, J. A review of dry (CO_2) reforming of methane over noble metal catalysts. *Chem. Soc. Rev.* **2014**, *43*, 7813–7837. [CrossRef]
21. Nikoo, M.K.; Amin, N.A.S. Thermodynamic analysis of carbon dioxide reforming of methane in view of solid carbon formation. *Fuel Process. Technol.* **2011**, *92*, 678–691. [CrossRef]
22. Özkara-Aydnolu, Ş. Thermodynamic equilibrium analysis of combined carbon dioxide reforming with steam reforming of methane to synthesis gas. *Int. J. Hydrogen Energy* **2010**, *35*, 12821–12828. [CrossRef]
23. Escudero, M.J.; Serrano, J.L. Individual impact of several impurities on the performance of direct internal reforming biogas solid oxide fuel cell using W-Ni-CeO_2 as anode. *Int. J. Hydrogen Energy* **2019**, *44*, 20616–20631. [CrossRef]
24. Chlipała, M.; Błaszczak, P.; Wang, S.F.; Jasiński, P.; Bochentyn, B. In Situ study of a composition of outlet gases from biogas fuelled Solid Oxide Fuel Cell performed by the Fourier Transform Infrared Spectroscopy. *Int. J. Hydrogen Energy* **2019**, *44*, 13864–13874. [CrossRef]
25. Liu, M.; van der Kleij, A.; Verkooijen, A.H.M.; Aravind, P.V. An experimental study of the interaction between tar and SOFCs with Ni/GDC anodes. *Appl. Energy* **2013**, *108*, 149–157. [CrossRef]
26. Ioannidou, E.; Chavani, M.; Neophytides, S.G.; Niakolas, D.K. Effect of the PH_2O/PCO_2 and PH_2 on the intrinsic electro-catalytic interactions and the CO production pathway on Ni/GDC during solid oxide H_2O/CO_2 co-electrolysis. *J. Catal.* **2021**, *404*, 174–186. [CrossRef]
27. Zhan, Z.; Lin, Y.; Pillai, M.; Kim, I.; Barnett, S.A. High-rate electrochemical partial oxidation of methane in solid oxide fuel cells. *J. Power Sources* **2006**, *161*, 460–465. [CrossRef]
28. Sun, C.; Stimming, U. Recent anode advances in solid oxide fuel cells. *J. Power Sources* **2007**, *171*, 247–260. [CrossRef]
29. Wang, W.; Jiang, S.P.; Tok, A.I.Y.; Luo, L. GDC-impregnated Ni anodes for direct utilization of methane in solid oxide fuel cells. *J. Power Sources* **2006**, *159*, 68–72. [CrossRef]
30. Wang, W.; Su, C.; Wu, Y.; Ran, R.; Shao, Z. Progress in solid oxide fuel cells with nickel-based anodes operating on methane and related fuels. *Chem. Rev.* **2013**, *113*, 8104–8151. [CrossRef]

31. Yue, W.; Li, Y.; Zheng, Y.; Wu, T.; Zhao, C.; Zhao, J.; Geng, G.; Zhang, W.; Chen, J.; Zhu, J.; et al. Enhancing coking resistance of Ni/YSZ electrodes: In Situ characterization, mechanism research, and surface engineering. *Nano Energy* **2019**, *62*, 64–78. [CrossRef]
32. Niakolas, D.K.; Neofytidis, C.S.; Neophytides, S.G. Effect of Au and/or Mo doping on the development of carbon and sulfur tolerant anodes for SOFCs-A short review. *Front. Environ. Sci.* **2017**, *5*, 78. [CrossRef]
33. Niakolas, D.K.; Athanasiou, M.; Dracopoulos, V.; Tsiaoussis, I.; Bebelis, S.; Neophytides, S.G. Study of the synergistic interaction between nickel, gold and molybdenum in novel modified NiO/GDC cermets, possible anode materials for CH_4 fueled SOFCs. *Appl. Catal. A Gen.* **2013**, *456*, 223–232. [CrossRef]
34. Neofytidis, C.; Dracopoulos, V.; Neophytides, S.G.; Niakolas, D.K. Electrocatalytic performance and carbon tolerance of ternary Au-Mo-Ni/GDC SOFC anodes under CH4-rich Internal Steam Reforming conditions. *Catal. Today* **2018**, *310*, 157–165. [CrossRef]
35. Neofytidis, C.; Ioannidou, E.; Sygellou, L.; Kollia, M.; Niakolas, D.K. Affecting the H_2O electrolysis process in SOECs through modification of NiO/GDC; experimental case of Au-Mo-Ni synergy. *J. Catal.* **2019**, *373*, 260–275. [CrossRef]
36. Ioannidou, E.; Neophytides, S.; Niakolas, D.K. Experimental clarification of the RWGS reaction effect in H_2O/CO_2 SOEC co-electrolysis conditions. *Catalysts* **2019**, *9*, 151. [CrossRef]
37. Neofytidis, C.; Ioannidou, E.; Kollia, M.; Neophytides, S.; Niakolas, D. The promoting effect of Fe on Ni/GDC for the Solid Oxide H_2O electrolysis. *Int. J. Energy Res.* **2020**, *44*, 10982–10995. [CrossRef]
38. Kan, H.; Lee, H. Enhanced stability of Ni-Fe/GDC solid oxide fuel cell anodes for dry methane fuel. *Catal. Commun.* **2010**, *12*, 36–39. [CrossRef]
39. Theofanidis, S.A.; Galvita, V.V.; Poelman, H.; Marin, G.B. Enhanced carbon-resistant dry reforming Fe-Ni catalyst: Role of Fe. *ACS Catal.* **2015**, *5*, 3028–3039. [CrossRef]
40. Theofanidis, S.A.; Batchu, R.; Galvita, V.V.; Poelman, H.; Marin, G.B. Carbon gasification from Fe-Ni catalysts after methane dry reforming. *Appl. Catal. B Environ.* **2016**, *185*, 42–55. [CrossRef]
41. Joo, S.; Seong, A.; Kwon, O.; Kim, K.; Lee, J.H.; Gorte, R.J.; Vohs, J.M.; Han, J.W.; Kim, G. Highly active dry methane reforming catalysts with boosted in situ grown Ni-Fe nanoparticles on perovskite via atomic layer deposition. *Sci. Adv.* **2020**, *6*, 35. [CrossRef] [PubMed]
42. Song, Z.; Wang, Q.; Guo, C.; Li, S.; Yan, W.; Jiao, W.; Qiu, L.; Yan, X.; Li, R. Improved effect of Fe on the stable $NiFe/Al_2O_3$ catalyst in low-temperature dry reforming of methane. *Ind. Eng. Chem. Res.* **2020**, *59*, 17250–17258. [CrossRef]
43. Zhang, T.; Liu, Z.; Zhu, Y.A.; Liu, Z.; Sui, Z.; Zhu, K.; Zhou, X. Dry reforming of methane on Ni-Fe-MgO catalysts: Influence of Fe on carbon-resistant property and kinetics. *Appl. Catal. B Environ.* **2020**, *264*, 118497. [CrossRef]
44. Zaravelis, F.; Sygellou, L.; Souvalioti, A.; Niakolas, D.K. Transition metals in Ni/GDC for the reversible solid oxide cell operation: Optimization of the Mo-Au-Ni synergy and further enhancement via substitution of Mo with Fe. *Electrochim. Acta* **2023**, *453*, 142343. [CrossRef]
45. Wu, Y.; Su, C.; Wang, W.; Wang, H.; Shao, Z. Effect of fabrication method on properties and performance of bimetallic $Ni_{0.75}$ $Fe_{0.25}$ anode catalyst for solid oxide fuel cells. *Int. J. Hydrogen Energy* **2012**, *37*, 9287–9297. [CrossRef]
46. HJeong; Kim, S.; Bae, Y.; Yoon, K.J.; Lee, J.; Hong, J. Effect of Fe infiltration to Ni/YSZ solid-oxide-cell fuel electrode on steam/CO_2 co-electrolysis. *Int. J. Energy Res.* **2019**, *43*, 4949–4958.
47. Simonsen, S.B.; Muhl, T.T.; Thydén, K.T.S.; Chatzichristodoulou, C.; Nielsen, J.; Sudireddy, B.R. Effect of Fe on high performing nanostructured Ni/Gd-doped ceria electrocatalysts. *Solid State Ion.* **2019**, *340*, 115019. [CrossRef]
48. Fiuza, P.R.; da Silva, M.A.; Boaventura, J.S. Development of Fe–Ni/YSZ–GDC electrocatalysts for application as SOFC anodes: XRD and TPR characterization and evaluation in the ethanol steam reforming reaction. *Int. J. Hydrogen Energy* **2010**, *35*, 11216–11228. [CrossRef]
49. Clementi, E.; Raimondi, D.L.; Reinhardt, W.P. Atomic screening constants from SCF functions. II. Atoms with 37 to 86 electrons. *J. Chem. Phys.* **1967**, *47*, 1300–1307. [CrossRef]
50. Majewski, A.J.; Singh, S.K.; Labhasetwar, N.K.; Steinberger-Wilckens, R. Nickel–molybdenum catalysts for combined solid oxide fuel cell internal steam and dry reforming. *Chem. Eng. Sci.* **2021**, *232*, 116341. [CrossRef]
51. Horváth, A.; Guczi, L.; Kocsonya, A.; Sáfrán, G.; La Parola, V.; Liotta, L.; Pantaleo, G.; Venezia, A. Sol-derived $AuNi/MgAl_2O_4$ catalysts: Formation, structure and activity in dry reforming of methane. *Appl. Catal. A Gen.* **2013**, *468*, 250–259. [CrossRef]
52. Mortensen, P.M.; Dybkjær, I. Industrial scale experience on steam reforming of CO_2-rich gas. *Appl. Catal. A Gen.* **2015**, *495*, 141–151. [CrossRef]
53. Fan, C.; Zhu, Y.A.; Xu, Y.; Zhou, Y.; Zhou, X.G.; Chen, D. Origin of synergistic effect over Ni-based bimetallic surfaces: A density functional theory study. *J. Chem. Phys.* **2012**, *137*, 014703. [CrossRef] [PubMed]
54. Ioannidou, E.; Neophytides, S.G.; Niakolas, D.K. Au-Mo-Fe-Ni/CeO_2 (Gd_2O_3) as Potential Fuel Electrodes for Internal CO_2 Reforming of CH_4 in Single SOFCs. *ECS Trans.* **2023**, *111*, 2473–2485. [CrossRef]
55. York, A.P.E.; Xiao, T.C.; Green, M.L.H.; Claridge, J.B. Methane oxyforming for synthesis gas production. *Catal. Rev.* **2007**, *49*, 511–560. [CrossRef]
56. Papadopoulou, C.; Matralis, H.; Verykios, X. Utilization of biogas as a renewable carbon source: Dry reforming of methane. In *Catalysis for Alternative Energy Generation*; Springer: New York, NY, USA, 2012; pp. 57–127.
57. Guilhaume, N.; Bianchi, D.; Wandawa, R.A.; Yin, W.; Schuurman, Y. Study of CO_2 and H_2O adsorption competition in the combined dry/steam reforming of biogas. *Catal. Today* **2021**, *375*, 282–289. [CrossRef]

58. Bradford, M.C.J.; Vannice, M.A. CO_2 reforming of CH_4. *Catal. Rev.* **1999**, *41*, 1–42. [CrossRef]
59. Fouskas, A.; Kollia, M.; Kambolis, A.; Papadopoulou, C.; Matralis, H. Boron-modified Ni/Al_2O_3 catalysts for reduced carbon deposition during dry reforming of methane. *Appl. Catal. A Gen.* **2014**, *474*, 125–134. [CrossRef]
60. Cesario, M.R.; Souza, G.S.; Loureiro, F.J.; Araújo, A.J.; Grilo, J.P.; Aouad, S.; Tidahy, H.L.; Macedo, D.A.; Fagg, D.P.; Gennequin, C.; et al. Synthesis of Co–Ni and Cu–Ni based-catalysts for dry reforming of methane as potential components for SOFC anodes. *Ceram. Int.* **2021**, *47*, 33191–33201. [CrossRef]
61. Huang, Y.; Du, J.; Ling, C.; Zhou, T.; Wang, S. Methane dehydrogenation on Au/Ni surface alloys-a first-principles study. *Catal. Sci. Technol.* **2013**, *3*, 1343–1354. [CrossRef]
62. Besenbacher, F.; Chorkendorff, I.; Clausen, B.S.; Hammer, B.; Molenbroek, A.M.; Nørskov, J.K.; Stensgaard, I. Design of a surface alloy catalyst for steam reforming. *Science* **1998**, *279*, 1913–1915. [CrossRef] [PubMed]
63. Kratzer, P.; Hammer, B.; Nørskov, J.K. A theoretical study of CH4 dissociation on pure and gold-alloyed Ni(111) surfaces. *J. Chem. Phys.* **1996**, *105*, 5595–5604. [CrossRef]
64. Li, L.; Anjum, D.H.; Zhu, H.; Saih, Y.; Laveille, P.V.; D'Souza, L.; Basset, J. Synergetic Effects Leading to Coke-Resistant NiCo Bimetallic Catalysts for Dry Reforming of Methane. *ChemCatChem* **2015**, *7*, 427–433. [CrossRef]
65. Bengaard, H.; Nørskov, J.; Sehested, J.; Clausen, B.; Nielsen, L.; Molenbroek, A.; Rostrup-Nielsen, J. Steam reforming and graphite formation on Ni catalysts. *J. Catal.* **2002**, *209*, 365–384. [CrossRef]
66. Shi, C.; Wang, S.; Ge, X.; Deng, S.; Chen, B.; Shen, J. A review of different catalytic systems for dry reforming of methane: Conventional catalysis-alone and plasma-catalytic system. *J. CO2 Util.* **2021**, *46*, 101462. [CrossRef]
67. Kim, S.M.; Abdala, P.M.; Margossian, T.; Hosseini, D.; Foppa, L.; Armutlulu, A.; van Beek, W.; Comas-Vives, A.; Copéret, C.; Müller, C. Cooperativity and dynamics increase the performance of NiFe dry reforming catalysts. *J. Am. Chem. Soc.* **2017**, *139*, 1937–1949. [CrossRef]
68. Wei, J.; Iglesia, E. Isotopic and kinetic assessment of the mechanism of reactions of CH_4 with CO_2 or H_2O to form synthesis gas and carbon on nickel catalysts. *J. Catal.* **2004**, *224*, 370–383. [CrossRef]
69. Jones, G.; Jakobsen, J.G.; Shim, S.S.; Kleis, J.; Andersson, M.P.; Rossmeisl, J.; Abildpedersen, F.; Bligaard, T.; Helveg, S.; Hinnemann, B.; et al. First principles calculations and experimental insight into methane steam reforming over transition metal catalysts. *J. Catal.* **2008**, *259*, 147–160. [CrossRef]
70. Kambolis, A.; Matralis, H.; Trovarelli, A.; Papadopoulou, C. Ni/CeO_2-ZrO_2 catalysts for the dry reforming of methane. *Appl. Catal. A Gen.* **2010**, *377*, 16–26. [CrossRef]
71. Akpan, E.; Sun, Y.; Kumar, P.; Ibrahim, H.; Aboudheir, A.; Idem, R. Kinetics, experimental and reactor modeling studies of the carbon dioxide reforming of methane (CDRM) over a new Ni/CeO_2-ZrO_2 catalyst in a packed bed tubular reactor. *Chem. Eng. Sci.* **2007**, *62*, 4012–4024. [CrossRef]
72. Luisetto, I.; Tuti, S.; Romano, C.; Boaro, M.; Di Bartolomeo, E. Dry reforming of methane over Ni supported on doped CeO_2: New insight on the role of dopants for CO_2 activation. *J. CO2 Util.* **2019**, *30*, 63–78. [CrossRef]
73. Bobrova, L.N.; Bobin, A.S.; Mezentseva, N.V.; Sadykov, V.A.; Thybaut, J.W.; Marin, G.B. Kinetic assessment of dry reforming of methane on Pt+Ni containing composite of fluorite-like structure. *Appl. Catal. B Environ.* **2016**, *182*, 513–524. [CrossRef]
74. Gavrielatos, I.; Drakopoulos, V.; Neophytides, S.G. Carbon tolerant Ni–Au SOFC electrodes operating under internal steam reforming conditions. *J. Catal.* **2008**, *259*, 75–84. [CrossRef]